

Investigation on Frequency Selective Surfaces for the Realization of Orientation Insensitive Indoor Localization Tag Landmarks

Untersuchung von frequenzselektiven Oberflächen zur Realisierung von orientierungsunabhängigen Positionsmarken für die Innenraumlokalisierung

Author:	Jesús Sánchez Pastor
Degree Programme:	M.Sc. Information and Communication Engineering
Examiner:	Prof. Dr.-Ing. Rolf Jakoby
Department:	Institut für Mikrowellentechnik und Photonik
Supervisor:	M. Sc. Alejandro Jiménez Sáez, Dr. Marta Cabedo Fabrés
Start Date:	24.10.2019
Date Of Submission:	23.04.2020
Examination Date:	07.05.2020
Masterthesis	(2299-M)



TECHNISCHE
UNIVERSITÄT
DARMSTADT



Affidavit/Eidesstattliche Versicherung

Erklärung zur Abschlussarbeit gemäß §22 Abs. 7 und §23 Abs. 7 APB TU Darmstadt.


Hiermit versichere ich, Jesús Sánchez Pastor, vorliegende Master-Thesis / Bachelor-Thesis gemäß §22 Abs. 7 APB der TU Darmstadt ohne Hilfe Dritter und nur mit den angegebenen Quellen und Hilfsmitteln angefertigt zu haben. Alle Stellen, die Quellen entnommen wurden, sind als solche kenntlich gemacht worden. Diese Arbeit hat in gleicher oder ähnlicher Form noch keiner Prüfungsbehörde vorgelegen. Mir ist bekannt, dass im Falle eines Plagiats (§38 Abs.2 APB) ein Täuschungsversuch vorliegt, der dazu führt, dass die Arbeit mit 5,0 bewertet und damit ein Prüfungsversuch verbraucht wird. Abschlussarbeiten dürfen nur einmal wiederholt werden. Bei der abgegebenen Thesis stimmen die schriftliche und die zur Archivierung eingereichte elektronische Fassung gemäß §23 Abs. 7 APB überein.

English translation for information purposes only:

Thesis Statement pursuant to §22 paragraph 7 and §23 paragraph 7 of APB TU Darmstadt I, Jesús Sánchez Pastor, herewith formally declare that I, Jesús Sánchez Pastor, have written the submitted thesis independently pursuant to §22 paragraph 7 of APB TU Darmstadt. I did not use any outside support except for the quoted literature and other sources mentioned in the paper. I clearly marked and separately listed all of the literature and all of the other sources which I employed when producing this academic work, either literally or in content. This thesis has not been handed in or published before in the same or similar form. I am aware, that in case of an attempt at deception based on plagiarism (§38 Abs. 2 APB), the thesis would be graded with 5,0 and counted as one failed examination attempt. The thesis may only be repeated once. In the submitted thesis the written copies and the electronic version for archiving are pursuant to §23 paragraph 7 of APB identical in content.

Darmstadt, den 23. April, 2020

Place, Date



Author

Zusammenfassung/Abstract

Die Lokalisierung und Positionierung von Zielen ist ein fortlaufendes Forschungsgebiet, das in den letzten Jahrzehnten aufgrund seiner zahlreichen Anwendungen in verschiedenen Bereichen wie Industrie, Gesundheit und Zivilbereich an Bedeutung gewonnen hat. Bei der präzisen Lokalisierung in Innenräumen kommt es vor allem darauf an, eine Auflösung im Sub-mm-Bereich zu erreichen, die durch den Betrieb im W-Band (65 GHz bis 110 GHz) und darüber aufgrund der großen verfügbaren Bandbreiten erreicht werden kann. Eine Implementierung solcher Systeme ist die Verwendung von Indoor-Tags, die als Landmarken oder Referenzpunkte dienen, so dass der Leser in der Lage ist, sie voneinander zu unterscheiden. Um dies zu erreichen, implementieren aktuelle passive Radarsysteme für Innenräume Frequenzmodulationsverfahren. Daher werden Tags durch frequenzselektive Oberflächen und Retroreflektoren gebildet, die die ankommende Abfrage-welle filtern und dann zum Sender zurückstreuen. Der derzeitige Stand der Technik solcher Systeme weist jedoch einige Einschränkungen auf, wie z.B. die Nichtresonanzstabilität bezüglich des Anregungswinkels und die Unbestimmtheit der Spiegelreflexion. In dieser Arbeit werden zwei Lösungen vorgeschlagen, um sie zu überwinden. Erstens werden vier klassische planare FSS mit Hilfe eines Gitters miniaturisiert, um eine stabile Resonanz zu erreichen. Sie werden als Teil einer Indoor-Tag-Landmarke hergestellt und gemessen, wobei die beste bei 79,30 GHz arbeitet und deren Resonanz innerhalb einer relativen Bandbreite von 2,22% variiert. Dies ermöglicht eine Auflösung von fünf Bit im W-Band. Zweitens, inspiriert durch das isotrope Verhalten von Metallkugeln, werden zwei schlitzbasierte halbkugelförmige FSSs mit Durchmessern von 15 mm und 20 mm aus Aluminium und Messing unter Verwendung von 3D-Drucktechniken hergestellt. Das Potenzial solcher Strukturen für die Arbeit an Lokalisierungssystemen in Innenräumen wird diskutiert, da beide das erforderliche Bandpassverhalten und das monostatische RCS-Minimum bei einer Betriebsfrequenz von 85 GHz aufweisen.

Target localization and positioning is an ongoing research area that has risen in importance during the last decades due to its numerous applications in several fields such as industrial, health and civilian. For precise indoor localization, the most important aspect is to achieve sub-mm resolution, which can be attained by operating in W-band (65 GHz to 110 GHz) and above due to the wide bandwidths available. One implementation of such systems is to use indoor tags that act as landmarks or reference points, that the reader is able to distinguish between each other. To achieve that, current indoor passive radar systems implement frequency modulation schemes. Therefore, tags are formed by frequency selective surfaces and retroreflectors, which filter the incoming interrogating wave and then backscatter it to the emitter. However, current state of the art of such systems present several limitations, like non-resonance stability regarding angle of excitation and specular reflection indetermination. In this work, two solutions are proposed to overcome them. First, four classical planar FSS are miniaturized using a grid to achieve stable resonance. They are fabricated and measured as part of an indoor tag landmark, with the best one operating at 79.30 GHz, and whose resonance varies within relative bandwidth of 2.22%. This allows for five bit resolution on W-band. Second, inspired in the isotropic behavior of metallic spheres, two slot-based semi spherical FSSs of diameters 15 mm and 20 mm are fabricated in aluminum and brass using 3D printing techniques. The potential of such structures to work on indoor localization systems is discussed, as both present the necessary bandpass behavior and RCS minimum at an operating frequency of 85 GHz.

Contents

1	Introduction	5
1.1	Indoor localization	5
1.2	Landmark recognition in frequency domain	6
1.3	Objective and structure of the work	7
2	Theoretical background	9
2.1	Basic radar parameters	9
2.1.1	Radar range equation	9
2.1.2	Radar range resolution	10
2.2	Radar cross-section (RCS) and retroreflectors	11
2.2.1	Definition and measurement of RCS	11
2.2.2	Retroreflectivity	12
2.3	Time gating technique	12
2.4	Frequency selective surfaces as filters	13
3	Planar Frequency Selective Surfaces with Angular-Stable Resonance	15
3.1	Oblique incidence in FSSs and resonance stability	15
3.2	Designed FSSs and characterization	16
3.2.1	Passband designs	17
3.2.2	Stopband designs	19
3.2.3	Fabricated structures and characterization	21
3.3	Planar FSS and corner reflector	27
3.3.1	Passband designs	27
3.3.2	Stopband designs	27
3.3.3	Discussion	30
4	Spherical FSS	33
4.1	Design challenges in spherical FSSs	33
4.1.1	Generation of complex structures with MATLAB and CST Studio Suite	34
4.2	Indoor tag landmark with spherical FSS and retroreflector	38
4.2.1	Designed FSSs	39
4.3	Fabricated structures and measured results	42
4.3.1	Bucky ball pattern FSS	43
4.3.2	Custom pattern FSS	45
4.3.3	Discussion	46
5	Conclusion and Outlook	49
A	Custom MATLAB - CST functions	51
B	Creation of cross-dipole in CST from MATLAB	53
C	Custom FSS pattern	55

Acronyms

CR corner reflector

DR dielectric resonator

ϵ_r relative dielectric permittivity

FSS frequency selective surface

GHz gigahertz

GNSS Global Navigation Satellite System

LOS Line-of-Sight

MHz megahertz

mm millimeter

PC photonic crystal

RCS Radar cross-section

TE₀₀ transversal electric planar wave

THz terahertz

TM₀₀ transversal magnetic planar wave

μm micrometer

μs microsecond

UWB ultra wide-band

VNA vector network analyzer

1 Introduction

1.1 Indoor localization

Target localization and positioning is an ever growing and ongoing research area. Currently, there is a widespread demand for accurate indoor positioning, since it allows for an increase in performance in automation and self-monitoring industrial processes. For instance, robots could move autonomously and freely within a building, foregoing current guiding systems such as fixed tracks or black stripes painted on the floor. Other indoor applications include end-user technologies in fields such as health, military, civilian, disaster relief and peacekeeping missions [1]. Main requirements of such systems are high precision, meaning sub-mm resolution; robustness, high refresh rate and sufficiently large reach.

Global Navigation Satellite System (GNSS) such as GPS, GLONASS or Galileo could be used to this purpose. However, these systems require direct Line-of-Sight (LOS) propagation, which makes them unsuitable for indoor environments, like offices or industrial buildings. Firstly, indoor accuracy requirements are higher than for outdoor environments. Secondly, radio signal attenuation caused by buildings has been reported to be on average 20-30 dBs higher than free space [2]. Thirdly, indoor environments are strongly dominated by propagation phenomena like reflection, scattering and diffraction, which are difficult to model and account for in radio propagation models [2]. Although indoor millimeter-resolution variations of GNSS such as Locata and iGPS are currently under development, they are limited by slow update rate and high cost [3].

In order to achieve successful indoor localization, one possibility is the use of *landmark tags*. The recognition of several of these tags allows the reader or robot moving inside the environment to position itself inside a common coordinate system using triangulation techniques. A generalized example of such system is depicted in Figure 1.1. In it, the reader is moving around while sending an interrogating signal (black lines). The tags answer actively or passively. The former means that the tags participate in the communication by sending information using their own antennas (cooperative radar system), while the latter implies that the interrogating signal is reflected back to the reader, without direct influence from the tags (passive radar system). Moreover, for this scenario the reader's transmitting and receiving antennas are located at the same place (mono-static radar).

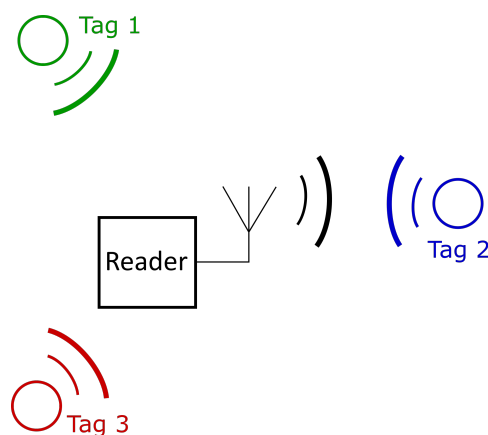


Figure 1.1: Sketch of generic indoor self-localizing system.

Current state of the art active indoor localization systems rely heavily in widespread technologies such as Wi-Fi, Zig-Bee and Bluetooth. Although cheap, these technologies are mainly located in the ISM band below 10 GHz, which means that their best achievable spatial resolution is in the order of centimeters, for the ones that are based on the ultra wide-band (UWB) spectrum. On the opposite, terahertz (THz) technologies have sub-mm spatial resolution, but suffer from high losses, which limits their reach. Between these two frequency ranges, the low THz band offers a good trade off between signal attenuation and absolute bandwidth, which means that it is possible to achieve reasonable reach with millimeter (mm) spatial resolution. Table 1.1 shows several currently used technologies and their achievable spatial resolution [4].

Physical Layer	Bandwidth	Resolution
802.11a/g Wi-Fi	20 MHz	15 m
802.11n Wi-Fi	40 MHz	7.5 m
802.11ac Wi-Fi	< 160 MHz	> 1.9 m
Ultra-wideband	> 500 MHz	< 60 cm
Low THz	80 GHz	3.75 mm

Table 1.1: Popular technologies and their spatial resolution [4]

The aforementioned technologies have the added drawback that they require a battery to work. This limits their effective lifetime and the maximum temperature in which they work accurately. Therefore, the use of passive surfaces to achieve detection is encouraged to solve these limitations. In conventional monostatic radar systems, passive detection means a radar system that can detect and track objects using the electromagnetic wave that is reflected on the object surface. Different approaches to achieve successful tag recognition in passive systems are to code the tag information in their backscattered response in frequency domain [5], time-domain [6], phase [7] or use hybrid coding techniques [8].

1.2 Landmark recognition in frequency domain

Encoding in frequency domain means to craft the reflected frequency-domain response of the tags so they are different and distinguishable. This can be achieved, for example, by employing dielectric resonator (DR) with different frequency responses [9] or resonators manufactured using photonic crystal (PC) slabs [5]. Nevertheless, both devices present decreasing RCS with high frequencies, which causes low receiving power, limiting the reach that they can achieve.

An alternative to the two aforementioned designs is to use frequency selective surface (FSS). FSSs are *planar and periodic arrays made from metallic patches or strips with different shapes* [10]. They present advantages regarding the previous structures such as higher gain and easiness of design and manufacturing. Figure 1.2 displays a potential landmark tag design based in the combination of FSS and corner reflector (CR) [11]. In this system, the reader sends an interrogating signal whose amplitude is the same for all frequencies. The FSSs present in Figure 1.2a are designed to be stopband, meaning that they reflect a certain frequency of the interrogating wave away from the reader, while letting the rest of the wave cross them. This resulting signal is then backscattered to the reader using trihedral corner reflector. The time- and frequency waveforms are displayed in 1.2b, where the frequency elimination is clear from the dip in received reflected signal.

The prior system has two main drawbacks. First, in case of frontal incidence the FSS reflects its working frequency back to the reader, where its merged with the reflection from the CR. Therefore, no landmark recognition is possible. Moreover, the operating frequency of the FSSs employed in this system is not stable, but it depends on the angle of incidence of the interrogating signal into the FSS. Depending whether the interrogating signal is transversal electric planar wave (TE₀₀) or transversal magnetic planar wave (TM₀₀), the operating frequency variations are up to 1% and 13%, respectively. For a TM₀₀ excitation, the tag needs a wide bandwidth to prevent its response from overlapping with other tags.

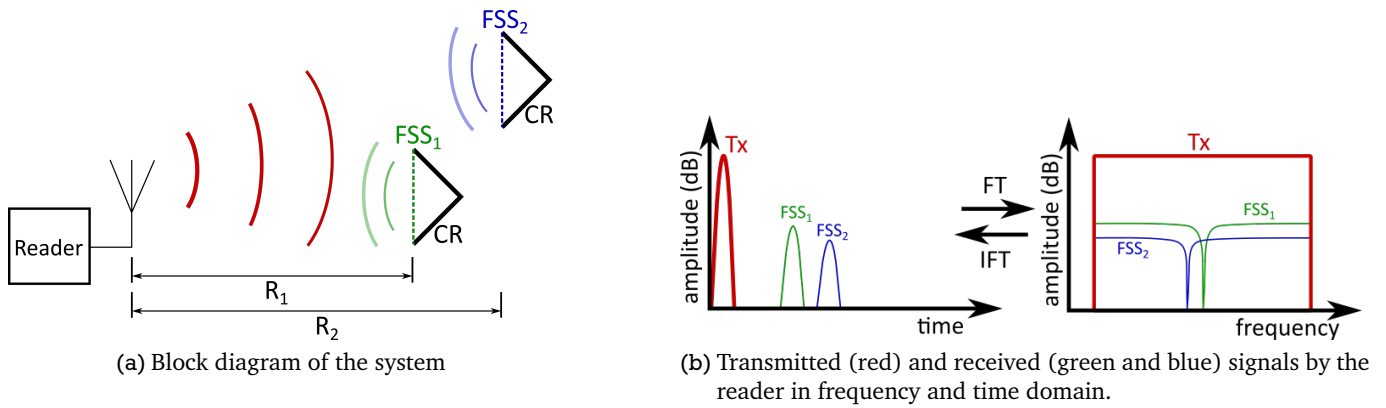


Figure 1.2: Self-localizing monostatic radar system in frequency domain, from [11]

1.3 Objective and structure of the work

In order to cope with the aforementioned issues in section 1.2, the goal of this work is to reduce the angular dependence of the system made by FSS and retroreflectors, both in amplitude and phase. On the one hand, it aims to design planar FSS with stable resonance for wide readout angles. On the other hand, it proposes a solution to both stable resonance and amplitude behavior by combining FSS and spherical retroreflectors. This latter approach also has the advantage of solving the frontal reflection indetermination.

This thesis is structured as follows: First, an overview of theoretical concepts often used in indoor localization is given in Chapter 2. Then, in Chapter 3, planar FSS with stable resonance are discussed, designed, fabricated and measured. Chapter 4 presents 3D-FSSs etched in metal spheres, as well as the design challenges that such structures bring. Moreover, it addresses its integration with ball lenses-based retro-reflectors. Finally, Chapter 5 presents a summary, conclusions and outlook of this work.



2 Theoretical background

This chapter presents and discusses basic radar concepts used in indoor localization systems. First, a variety of radar terms such as the radar range equation and radar cross section are explained. Then, topics specific of frequency selective surfaces with retroreflectors are addressed. Also, the use of time gating in highly cluttered scenarios is discussed.

2.1 Basic radar parameters

When considering an indoor localization scenario, radar range and radar resolution are two relevant parameters that define the ability of the system to detect and distinguish between tags. In this work, the transmitting and receiving antennas are situated at the reader, and the landmark tags act as a reflective passive structure. Therefore, this system can be considered as a mono-static radar system and is treated as such in the following theory.

2.1.1 Radar range equation

The radar range defines the maximum achievable separation between reader and tag that allows the mono-static radar to receive a response above the noise floor i.e. to detect its target. According to Skolnik [12, Chapter 1], for a direct LOSs and free-space scenario, the received power by the radar is given by

$$P_r = \frac{P_t G^2 \lambda^2 \sigma}{(4\pi)^3 R^4} \quad (2.1)$$

where:

- P_r = Received power at the reader.
- P_t = Transmitted signal power at the reader.
- G = Gain of the reader antenna.
- λ = Transmitted wavelength.
- σ = Radar-Cross Section (RCS) of the tag landmark.
- R = Distance between reader and tag.

Equation 2.1 exposes that the radar signal attenuates by a factor of R^4 as it travels forth and back from a tag at distance R . In order to obtain the maximum range, R_{\max} , the previous received power, P_r , is substituted by the minimum detectable power at the receiver, S_{\min} , which can be expressed as [12]:

$$S_{\min} = \frac{S}{N} K T_0 B N_F \quad (2.2)$$

where:

S/N = signal to noise ratio at the receiver.
 KT_0BN_F = thermal noise power.
 K = Boltzmann 's constant.
 T_0 = Temperature of the receiver.
 B = Noise bandwidth of the receiver.
 N_F = noise figure of the receiver.

Equations 2.1 and 2.2 can be combined and solved in terms of R to obtain the radar range equation, which gives insight about the maximum distance that a landmark tag can be reliably detected.

$$R_{\max} = \sqrt[4]{\frac{P_t G^2 \lambda^2 \sigma}{(4\pi)^3 K T_0 B N_F \frac{S}{N}}} \quad (2.3)$$

A direct consequence of equation 2.3 is that the range of a certain radar can be doubled by increasing the signal to noise ratio by 12 dB, which is achieved by increasing the transmitted power by a factor of 16.

2.1.2 Radar range resolution

Range resolution is the capability of radar system to successfully differentiate two scatterers that are very close to each other. It is mainly dependent on the width of transmitted pulse: the narrower the pulse in time domain, the higher the resolution that can be achieved. For a monostatic radar, this magnitude is given by [13, Chapter 13]:

$$S_r \geq \frac{c_0 \tau}{2} = \frac{c_0}{2B} \quad (2.4)$$

where,

S_r = Range resolution, meaning minimum detectable separation between scatterers.
 τ = Transmitted pulse width.
 B = Bandwidth of the transmitted signal.

As an example, a signal with pulse width of 1 microsecond (μs) (1 megahertz (MHz) bandwidth) has a range resolution of 150 meters, which puts into relevance the need of shorter signals (wide frequency ranges) in time domain for indoor localization environments.

Equation 2.3 assumes that there is a direct path between radar and target. However, this becomes increasingly difficult in indoor environments, that are characterized by having dense multipath characteristics. Since the indoor localization system proposed in Chapter 1 depends on angle of arrival of the scattered signal, proper direct path detection is critical to self-positioning in order to prevent early false alarm errors and missed path errors. As shown in equation 2.4, a transmitted signal with infinitely large bandwidth provides finer time resolution, enabling higher multi path resolution and ranging accuracy. In reality, a bandwidth of 4 GHz is enough to achieve direct path accurate detection with centimeter resolution in indoor environments, as shown for a system working at 12.5 gigahertz (GHz) in [14].

2.2 RCS and retroreflectors

2.2.1 Definition and measurement of RCS

Radar cross section (RCS) is the portion of radiated power that is incident on a target, which is radiated toward the receiving antenna of a radar, which is written as [13, Chapter 17]

$$\sigma = \lim_{R \rightarrow \infty} 4\pi R^2 \left| \frac{E_r}{E_i} \right|^2 \quad (2.5)$$

This definition implies that the incident wave on the target is a plane wave, since σ is defined for $R = \infty$. RCS can be classified in bistatic RCS, when the emitting and receiving antennas are separated in space; or monostatic RCS, when both antennas are located together. As aforementioned, this latter value is the one of interest for the indoor localization system presented in this document. Both RCS possibilities are related with

$$RCS_{\text{mono}} = RCS_{\text{bistatic}}(\theta = 0, \varphi = 0) \quad (2.6)$$

where θ denotes elevation angle and φ azimuth of the antenna. In this case, both angles being zero refers to direct path between antenna and target.

Although the RCS of a target could be obtained using Equation 2.1, a precise calculation for a wide frequency range is costly. The accurate estimation of critical parameters such as antenna gain and reader-tag distance is difficult. Moreover, this approach requires to guarantee that there is only LOS contribution, as assumed in equation 2.1. An easier approach to measure RCS is to use a reference object with known RCS and divide equation 2.1 by itself, but with different received powers and RCSs, resulting:

$$\frac{\sigma_{\text{target}}}{\sigma_{\text{ref}}} = \frac{P_{\text{target}}}{P_{\text{ref}}} \quad (2.7)$$

where,

- σ_{target} = RCS of the target object.
- σ_{ref} = RCS of the reference object.
- P_{target} = Back-scattered power density from the target detected by the radar.
- P_{ref} = Back-scattered power density from the reference detected by the radar.

When using a vector network analyzer (VNA), P_{ref} and P_{target} might be replaced by the corresponding measured scattering matrix parameters. A complete definition and explanation about these parameters can be found in [15, Chapter 4]. Concretely, in the case of monostatic RCS the only scattering parameter that needs to be measured is S_{11} , also known as reflection coefficient. Thus, Equation 2.7 reduces to:

$$\frac{\sigma_{\text{target}}}{\sigma_{\text{ref}}} = \frac{S_{11,\text{target}}}{S_{11,\text{ref}}} \quad (2.8)$$

To apply the previous equation it is assumed that all parameters but receiving power remain constant for both measurements. Furthermore, the reference object must have a well known RCS, or one that is possible to calculate with a theoretical formula. Although there are several possibilities of such objects such as flat rectangular plates, top hat or cylindrical reflectors [16], one easy to manufacture and well studied reflector is the metallic sphere. Using this object as reference has two main advantages. First, metal sphere's RCS is stable when measured in its optical scattering region [17] [18]. Second, its scattered response is omnidirectional, which eliminates needing a precise alignment between reference and antenna to achieve

frontal incidence. For instance, the RCS of a square and conducting metal plate experiments variations of around 30 dB depending of angle of incidence. [13, Chapter 17]

2.2.2 Retroreflectivity

Retroreflectors are objects that backscatter an incident wave in the same direction of arrival with minimum deviation. In layman terms, they *send back* the incident signal to the transmitter. The main difference between these devices and a planar mirror is that, while the former always reflect incident waves towards the source, the latter presents specular reflection. In other words, incident wave is reflected with an angle equal to angle of incidence. They only present retroreflection when incident wave is perpendicular to mirror's surface. Figure 2.1a sketches these differences, while 2.1b displays the four most common used retro reflectors nowadays.

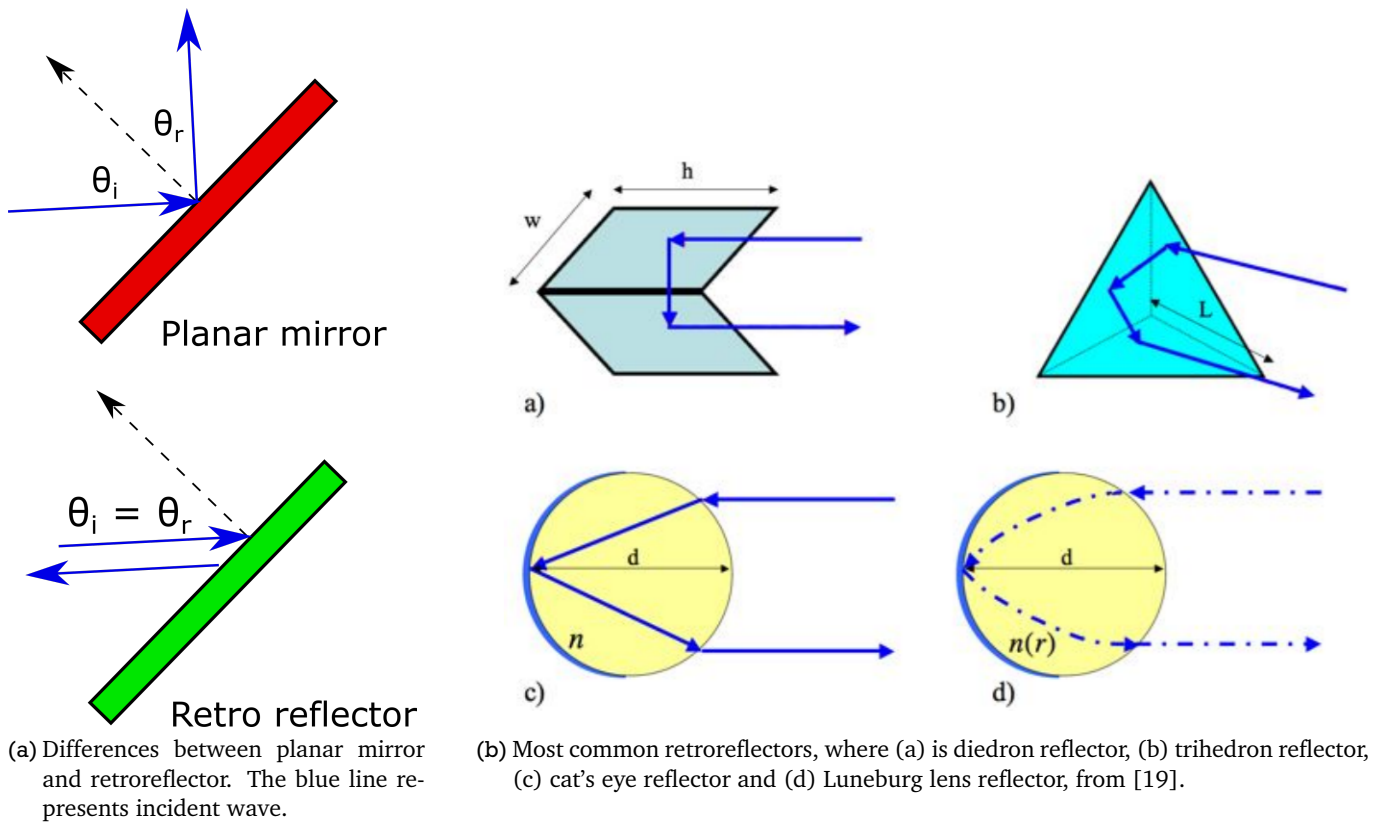


Figure 2.1: Differences between mirror and retroreflectors and most common retroreflectors.

In this work, a trihedral corner reflector and cat's eye reflector are used in combination with FSSs.

2.3 Time gating technique

In real world scenarios, the received signal might include unwanted reflections not only from the desired target, but also from nearby objects, which are called clutter. This is of great relevance in indoor situations, that are highly cluttered. A transmitted signal is scattered in those scenarios, which in turn results in a noisy received signal, up to the point where no resonance is distinguishable. A technique to remove these unwanted influences is Time Gating. It consists to window a signal in time domain, which later can be transformed to frequency domain. This way, only the time data corresponding to the resonator response is used and the initial distortion originated from the scenario is cleaned from the received signal, improving the

quality of the response. Notwithstanding, this technique is applied to eliminate reflections of objects away from the target or in resonators with sufficiently high quality factors, in order for their response to outlast the environmental scatterers. Figure 2.2 sketches how this technique works. An example of its successful use in wireless pressure sensors is found in [20].

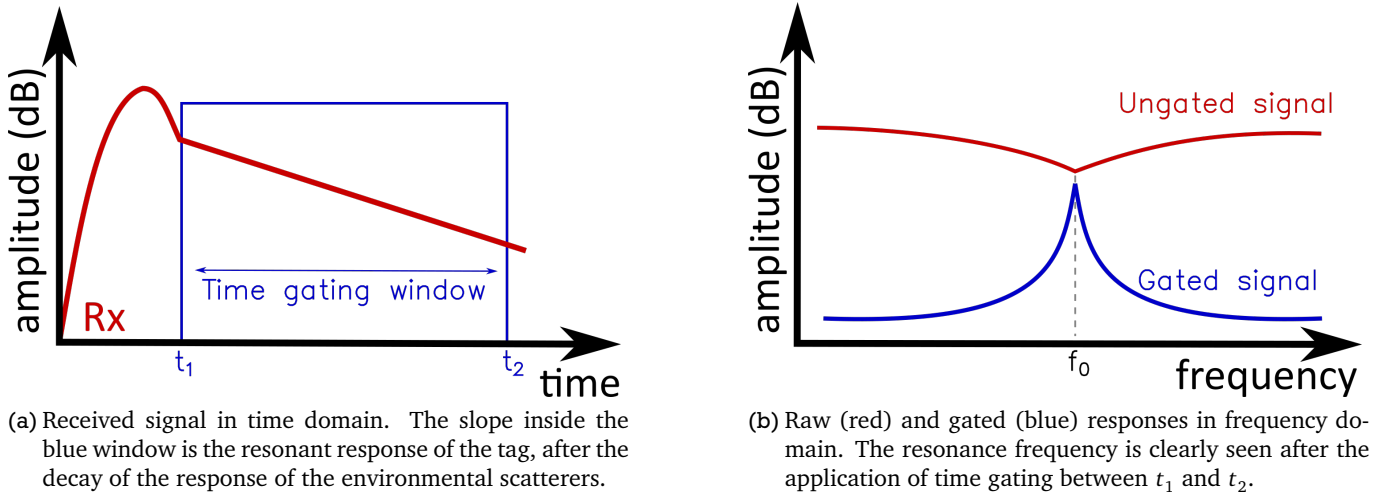


Figure 2.2: Sketch of time gating technique

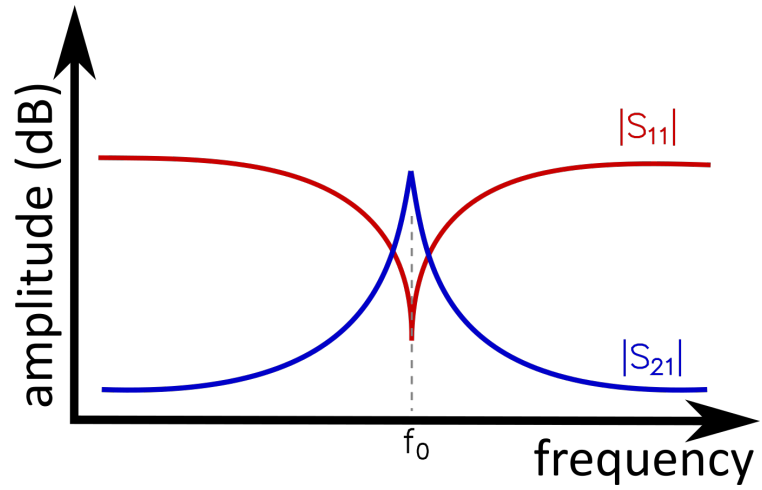
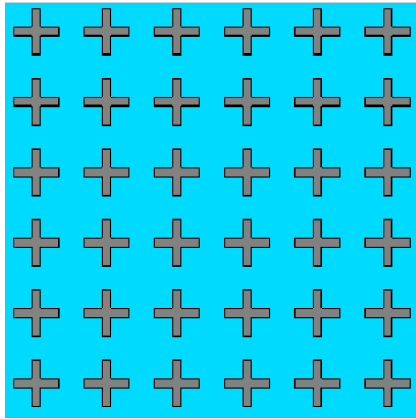
As aforementioned, to achieve a successful recognition of the resonating frequency of the landmark tag, the resonance needs to outlast the clutter response of environment. However, FSS do not have high-Q factors, a problem that can be partially bypassed by employing low-loss homogeneous dielectric lenses, which also show high-Q resonances, such as the ones presented in section 2.2.

2.4 Frequency selective surfaces as filters

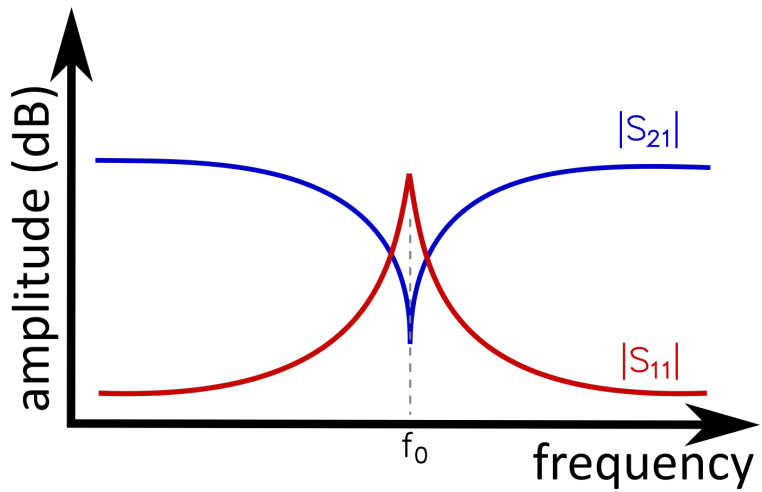
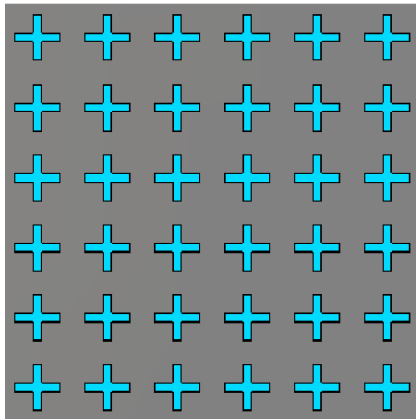
FSSs are thin structures of 1-D or 2-D periodically distributed resonating elements that are designed to transmit, absorb or reflect electromagnetic waves at a certain frequency. They are usually made by arranging thin metal elements in certain periodic lattices into a dielectric support. The complementary option, the use of apertures in a conducting plane, is also a valid option to create FSSs [10]. The periodicity present in these structures simplifies their electromagnetic analysis and simulation, since only one unit cell of the structure needs to be considered when applying Floquet's theorem [21].

The features of such FSSs mainly depend on the separation between unit cells and the shape of their basic elements. In order to have only the fundamental mode propagating through the structure, periodicity needs to fulfill the condition $\min(p_x, p_y) \leq \lambda_0/2$, where p_x, p_y are the lattices in X and Y directions, considering a propagating wave in Z-axis, and λ_0 the operating frequency. Furthermore, a wide range of basic unit cells exist, which are used in different applications such as hexagonal loops for frequency selective windows [22], square and circular loops for imaging techniques [23] or circular aperture patches in double band reflect-array structures [24].

FSSs can be classified as active or passive, depending on whether they need biasing (e.g. power) or not, respectively. In this work, passive FSSs are employed, meaning that they are designed to work at a certain frequency. On the one hand, when a FSS is made by metallic elements, it usually exhibits stopband behavior. On the other hand, when it is formed by apertures, it shows passband response. An example of these possibilities is displayed in figure 2.3, with their corresponding scattering parameters.



(a) Bandstop FSS. The structure is displayed in left side, made of thin metallic cross-dipoles (gray) on a substrate (blue) whereas right side shows ideal scattering parameters.



(b) Bandpass FSS. The structure is displayed in left side, made from aperture elements on a metallic plane (gray) on a substrate (blue) whereas right side shows ideal scattering parameters.

Figure 2.3: Bandstop and bandpass FSS using cross-dipoles.

3 Planar Frequency Selective Surfaces with Angular-Stable Resonance

As discussed in section 1.2, it is desirable that tag landmarks have stable resonance frequency, which is independent of angle of arrival of interrogating signal. However, this feature is not present on most basic unit cells. This chapter aims to explain the reasons behind this behavior, as well as to propose solutions to it. The orientation-insensitive designed structures are measured in an similar set up to the one presented in figure 1.2. Moreover, their performance in terms of resonance stability is compared with the results presented in [11].

3.1 Oblique incidence in FSSs and resonance stability

FSS design techniques rely in the excitation of the structure by an incoming planar wave, normal to FSS surface. However, this is a scenario that does not usually happen in real world applications, where the incoming wave usually has a oblique angle regarding FSS, which modifies the resonant frequency of the structure. Although an exact relation between spectral behavior and angular incidence is difficult to achieve without the use of full electromagnetic wave simulations, it is possible to describe the general behavior of FSS made up from basic elements [25]. The change in frequency domain behavior depends on whether the incident wave is TE-polarized or TM-polarized. A depiction of both scenarios is displayed in figure 3.1, where DOP means direction of propagation, denoted by black arrows. Blue arrows indicate electric field and green arrows magnetic field. Finally, θ and φ denote the angle of incidence for TE and TM wave, respectively.

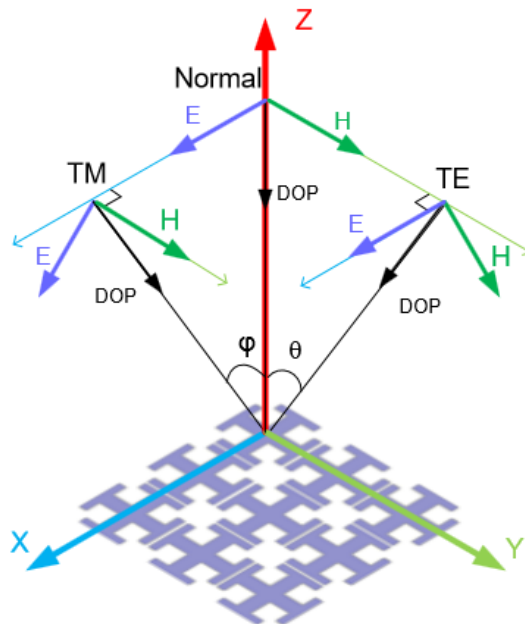


Figure 3.1: Illustration of TE and TM incidence, from [25].

- **TM incidence:** Corresponding to the scenario drawn on the left part of figure 3.1, it is characterized by having the magnetic field parallel to FSS surface and electric field impinging with a certain angle φ . Therefore, only a fraction of the electric field is normal to the surface, $\vec{E}_{\text{normal}} = \vec{E} \cdot \cos(\varphi)$. Larger incident angles generate larger phase differences between adjacent elements of the FSS. This in turn causes increasingly resonance dampening [26].
- **TE incidence:** Corresponding to the scenario drawn on the right part of figure 3.1, it is characterized by having the electric field parallel to FSS surface and magnetic field impinging with a certain angle φ . Therefore, only a fraction of the magnetic field is normal to the surface, $\vec{H}_{\text{normal}} = \vec{H} \cdot \cos(\varphi)$. The incident angle induces phase differences along the FSS-axis, which increases the electrical size of the structure, shifting its resonance frequency to lower parts of the spectrum, but without modifying its bandwidth [27].
- **Oblique incidence:** Not represented, both electric and magnetic field have a certain angle while impinging in the structure. The aforementioned behaviors are thus mixed, namely resonance shifting and dampening.

In light of the above, resonance stability is achieved when the excited phase differences in each element along the FSS are minimized. The less contrast between excited phases, the more stable the structure is regarding its angular behavior. There are mainly three approaches to achieve this effect in 2D FSS.

1. **Minimize spacing between elements** by orientating them properly. One example is the Cassegrain subreflector designed by Agrawal and Imbriale [28], which features a cross-dipole FSS whose elements are rotated 45° compared to the example in figure 2.3. By doing so, reasonable angle stability is achieved up to 60° .
2. **Miniaturize elements**, which decreases whole FSS size regarding operating wavelength. This in turn reduces excited phase differences along FSS' axis. For instance, fractal elements [29] or double square ring slots [30] have shown good angular stability for both TE and TM polarized waves up to 60° . Furthermore, extremely complex structures such as the one presented in [31] also shown good resonance stability. Another possibility is the inclusion of a grid in the FSS [27] [32] [33].
3. **Use layered FSS.** For instance, surrounding the FSS with two layers of dielectric material. Due to Schnell's law, incident wave is reflected closer to structure axis, as it's relative dielectric permittivity (ϵ_r) constant is higher than air [34]. This approach is better suited for TE excitations, as TM incidences present limitation of Brewster angle [27]. Finally, multi-layered FSS also offer good resonance stability [35].

Further designs that achieve resonance stability regarding incident wave are 3D FSS, which rely in the combination of 2D surface FSS resonance with a cavity mode that arises when FSS has height. These structures have reportedly achieved resonance stability for both TE and TM excitation up to 80° [36]. However, they rely in fabricating the structure in dielectric support and then spraying the parts where metal is desired with an aerosol. Although a good option, precise spraying of the structure is difficult to achieve at 85 GHz due to the small dimensions of the designs.

From the aforementioned approaches, the chosen one in this work is to combine square- and ring element unit cells with a grid, as presented in section 3.2.

3.2 Designed FSSs and characterization

The approach chosen in this work to achieve resonance stability regarding angle of incidence is to miniaturize two classical FSS' unit cells by using a grid. The two designs selected are square ring and circular ring type FSSs. Moreover, their complementary designs are also studied, as the former present passband response regarding operating frequency, whereas the latter shows stopband behavior.

The available W-band measurement setup is able to characterize devices from 65 GHz to 110 GHz. For this reason, the FSSs are designed with a resonance frequency of 85 GHz, so that characterization of the behavior before and after the resonance is possible even if some frequency shifts occur in the manufacturing process. The chosen substrate to implement the FSS is Rogers RT 5880 with a substrate height of 0.127 mm, due to his availability, cost and easiness to manufacture metal structures onto it. Moreover, its dielectric permittivity, ϵ_r is 2.2, which decreases the influence of having high ϵ_r materials in resonance stability, as mentioned in section 3.1. Finally, the metalization on structures is copper of 0.035 mm height. In simulations, PEC is used instead.

Simulations are performed with CST Microwave Studio, using a pre-defined template for planar 2D-FSS, which uses Floquet excitation and sets boundary conditions to periodic, simulating a periodic, infinite environment. This allows for the design of only one unit cell of the FSS, while obtaining the whole structural response. The main difference between Floquet and waveguide port simulations is how the reflection and transmission coefficient are labeled. While in the latter only one wave is propagated, in the former the response for both TE00 and TM00 polarized waves is presented, which are identified with a (1) and (2) in simulation results, respectively. Furthermore, due to the difference in excitation, reflection and transmission coefficient are not labeled as scattering parameters, but using Floquet port configuration, which are called Z_{\max} and Z_{\min} . In this work, only Z_{\max} port is used as source of excitation. Thus, reflection coefficient for TE00-polarized wave is denoted as $SZ_{\max}(1), Z_{\max}(1)$ and transmission coefficient is represented by $SZ_{\min}(1), Z_{\max}(1)$. For TM00 excitation the notation difference is that its results have a (2) instead of a (1).

3.2.1 Passband designs

As aforementioned, two classical FSS unit cells are used and inserted into a gridded structure, which are square ring and circular ring.

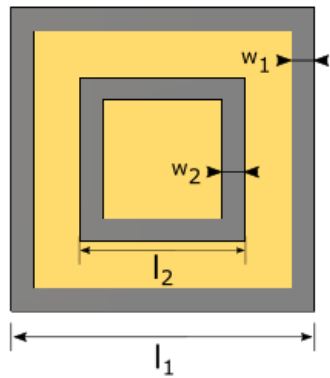
Gridded square ring FSS

The designed unit cell is displayed in 3.2a, with its design parameters presented on table 3.1. Figure 3.2b presents its reflection and transmission coefficient using the previously mentioned Floquet notation. Since the structure is perfectly symmetric in both axis, TE00 and TM00 response for frontal excitation overlap. The operating frequency of the structure is 84 GHz, which is measured taking into account the minimum presented in the reflection coefficient.

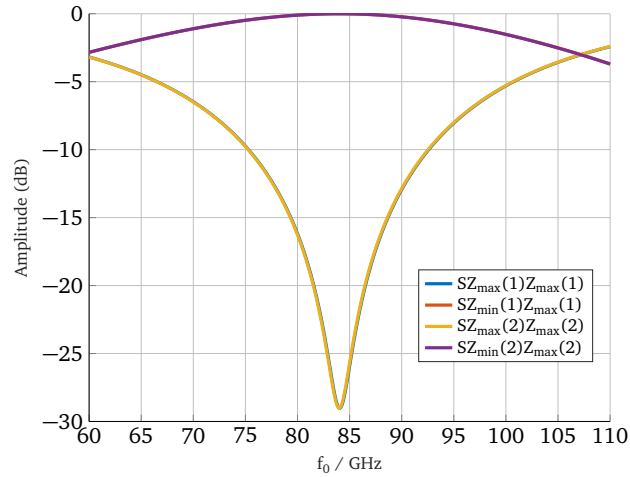
	in mm
Grid length, l_1	1.32
Grid width, w_1	0.1
Ring length, l_2	0.72
Ring width, w_2	0.1

Table 3.1: Dimensions of gridded square ring unit cell.

As mentioned in section 3.1, by using a grid the distance between FSS' unit cells is decreased, which in turns increases its resonance stability. Figure 3.3a displays a scaled comparison between the designed gridded structure and a normal square ring unit cell. The former is around 42% smaller than the latter. Moreover, their simulated resonance frequency regarding angle of excitation for TE00 and TM00 polarized waves is presented in figure 3.3b and c, respectively. For TE00 excitation, the response of the classical square ring falls rapidly after 10° . However, the same does not happen for its gridded counterpart. It presents significantly



(a) Gridded square type unit cell. PEC is represented as gray color and substrate as orange.



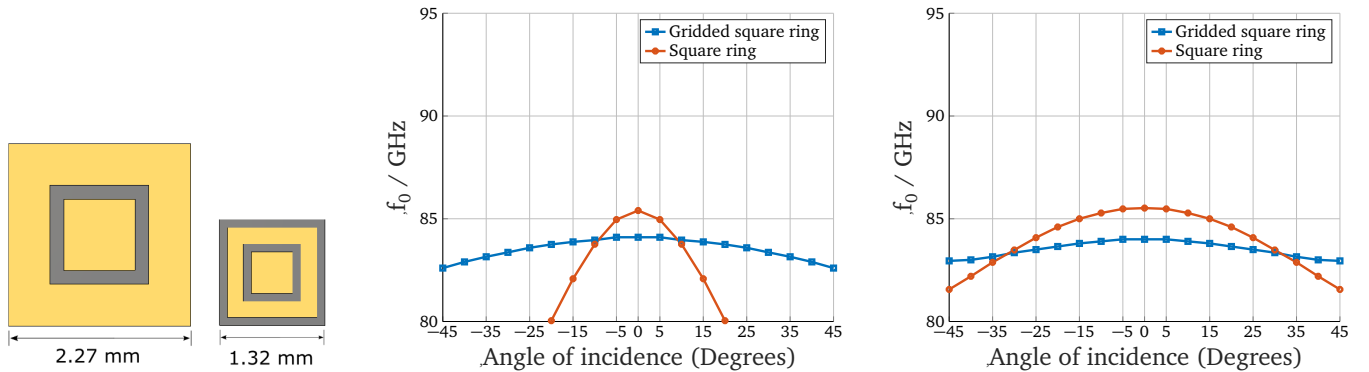
(b) Reflection and transmission response for both TE00 and TM00 excitations. From the graph, this structure presents passband behavior at 84 GHz for both polarizations.

Figure 3.2: Designed gridded square ring FSS and its response.

larger angular stability up to 45°. While at normal incidence its resonance frequency is 84 GHz, it decreases to 82.6 GHz for 45° incidence. This means a resonance shift Δf of 1.6% , computed as

$$\Delta f (\%) = 100 \cdot \frac{f_0 - f_{\theta = 45^\circ}}{f_0} \quad (3.1)$$

where f_0 is frontal incidence response and θ represents angle of incidence.



(a) Square ring type. Gridded FSS unit cell (right) is around 42% smaller than normal FSS unit cell (left).

(b) TE00 excitation. Square markers correspond to gridded FSS type, whereas circular markers to normal FSS.

(c) TM00 excitation. Square markers correspond to gridded FSS type, whereas circular markers to normal FSS.

Figure 3.3: Comparison between classical square ring and gridded design regarding resonance stability.

The resonance frequency of classical square ring is more stable for TM00 excitation than TE00 excitation, with $\Delta f = 4.6\%$ resonance shift. As explained in section 3.1, the main influence in TM00 excitation is not resonance shift, but resonance damping. Nevertheless, the gridded option is even better, presenting $\Delta f = 1.2\%$, which is slightly smaller than when excited by a TE00-polarized wave.

Gridded circular ring FSS

The designed unit cell is displayed in figure 3.4a, with its design parameters presented on table 3.2. Figure 3.4b presents its reflection and transmission coefficient using the previously mentioned Floquet notation. Since the structure is perfectly symmetric in both axis, TE₀₀ and TM₀₀ response for frontal excitation overlap. The operating frequency of the structure is 85.20 GHz, which is measured taking into account the minimum presented in the reflection coefficient.

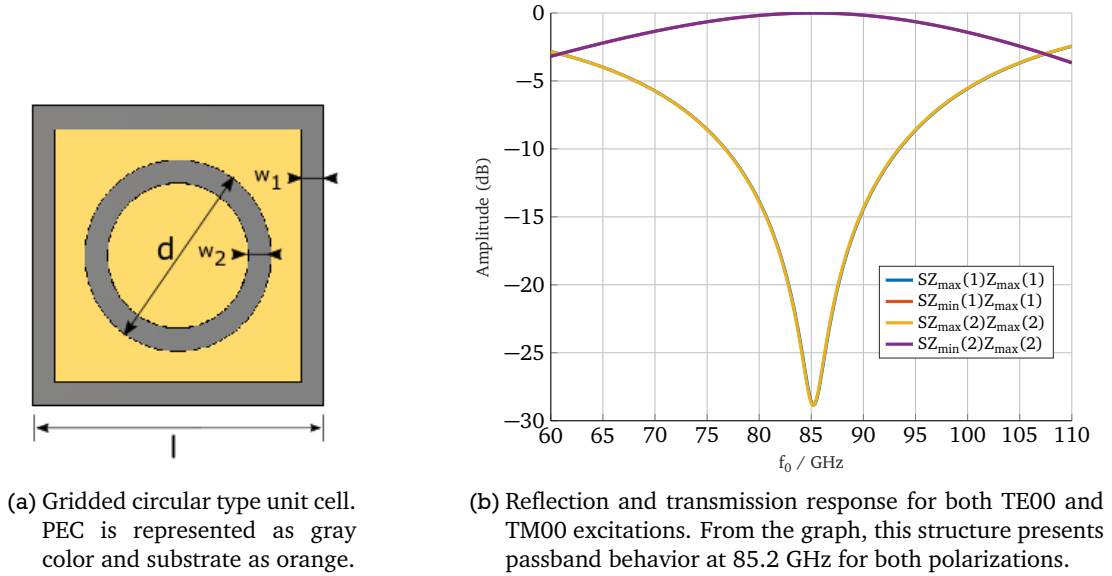


Figure 3.4: Designed gridded circular ring FSS and its response.

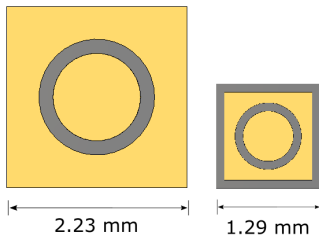
	in mm
Grid length, l	1.2875
Grid width, w_1	0.1
Ring diameter, d	0.824
Ring width, w_2	0.1

Table 3.2: Dimensions of gridded circular ring unit cell.

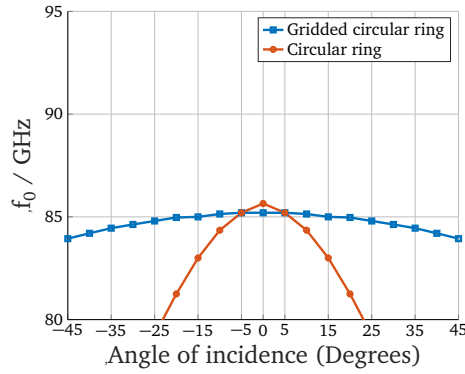
Regarding its size compared to the classical circular ring UC, figure 3.5 a displays a scaled comparison between both of them. The gridded design is around 42% smaller than the classical one. Moreover, their simulated resonant frequency regarding angle of excitation for TE₀₀ and TM₀₀ polarized waves is presented in figure 3.3 b and c, respectively. As expected, the gridded option has a more stable resonance regarding angle of incidence, presenting a frequency shift Δf of 1.48% and 1.40% for TE₀₀ and TM₀₀ excitation, respectively.

3.2.2 Stopband designs

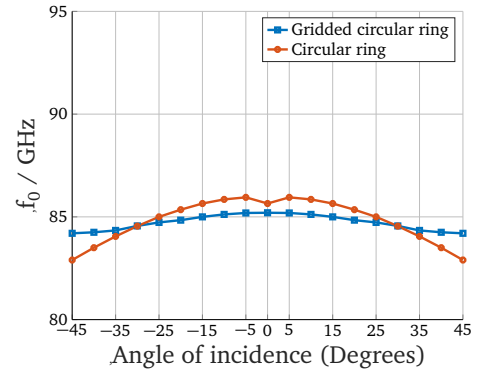
The stopband designs are the complementary structures of the ones previously presented. Following Babinet's principle, this means that the frequency behavior is inverted, while maintaining the same resonant frequency. Although they present stopband behavior, their operating frequency shifted 5 GHz towards higher frequencies. This is because the structures have a certain thickness, whereas Babinet principle is formulated for infinitely thin structures. Nevertheless, the dimensions are not resized, and thus are the same presented in tables 3.1 and 3.2



(a) Circular ring type. Gridded FSS unit cell (right) is around 42% smaller than normal FSS unit cell (left).



(b) TE₀₀ excitation. Square markers correspond to gridded FSS type, whereas circular markers to normal FSS.

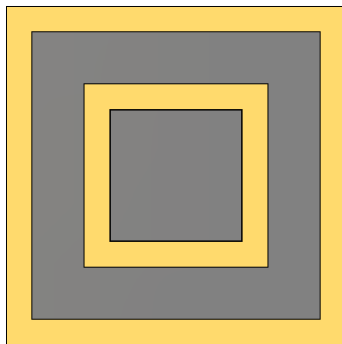


(c) TM₀₀ excitation. Square markers correspond to gridded FSS type, whereas circular markers to normal FSS.

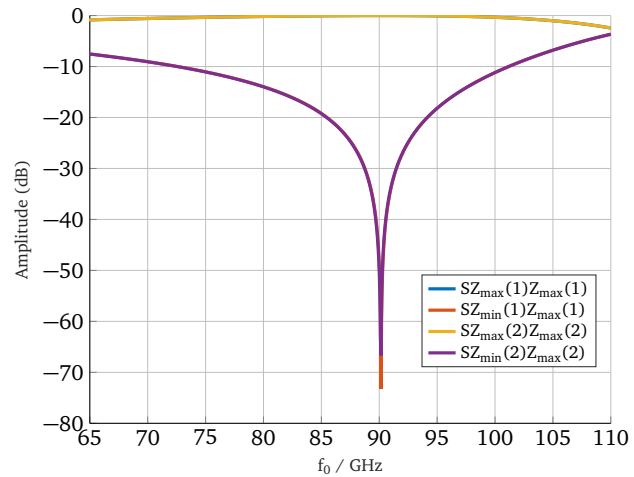
Figure 3.5: Comparison between classical circular ring and gridded design regarding resonance stability.

Complementary gridded square ring FSS

The designed unit cell is displayed in 3.6 a, with its design parameters presented on table 3.1. Figure 3.6 b presents its reflection and transmission coefficient using the previously mentioned Floquet notation. Since the structure is perfectly symmetric in both axis, TE₀₀ and TM₀₀ response for frontal excitation overlap. The operating frequency of the structure is 90 GHz, which is measured taking into account the minimum presented in the transmission coefficient.



(a) Gridded square type unit cell. PEC is represented as gray color and substrate as orange.



(b) Reflection and transmission response for both TE₀₀ and TM₀₀ excitations. From the graph, this structure presents stopband behavior at 90.15 GHz for both polarizations. Moreover, their responses perfectly overlap for normal incidence.

Figure 3.6: Designed complementary gridded square ring FSS and its response.

Regarding its comparison with the complementary square ring unit cell, figure 3.7 a displays a size comparison between both of them. The gridded design is around 31% smaller than the classical one. This variation is not the same as the one between passband designs, owing to the classical complementary unit cell having a resonant frequency around 75 GHz. Thus, its size is scaled to work at around 85 GHz for comparison purposes. Their simulated resonant frequency regarding angle of excitation for TE₀₀ and TM₀₀ polarized

waves is presented in figure 3.3 b and c, respectively. Interestingly, the resonance shift for TE₀₀ excitation is the same for both classical and gridded options, around 5% and 4%, respectively. This is due to the presence of the metallic plane, that prevents capacitive coupling between FSS' elements. Thus, the resonant frequency of the FSS depends mainly on the frequency shift that each element experiments when excited with different incident waves. Regarding TM₀₀ excitation, the gridded option presents a relative shift of 0.44%, whereas the classical unit cell has a frequency shift of 5.7%.

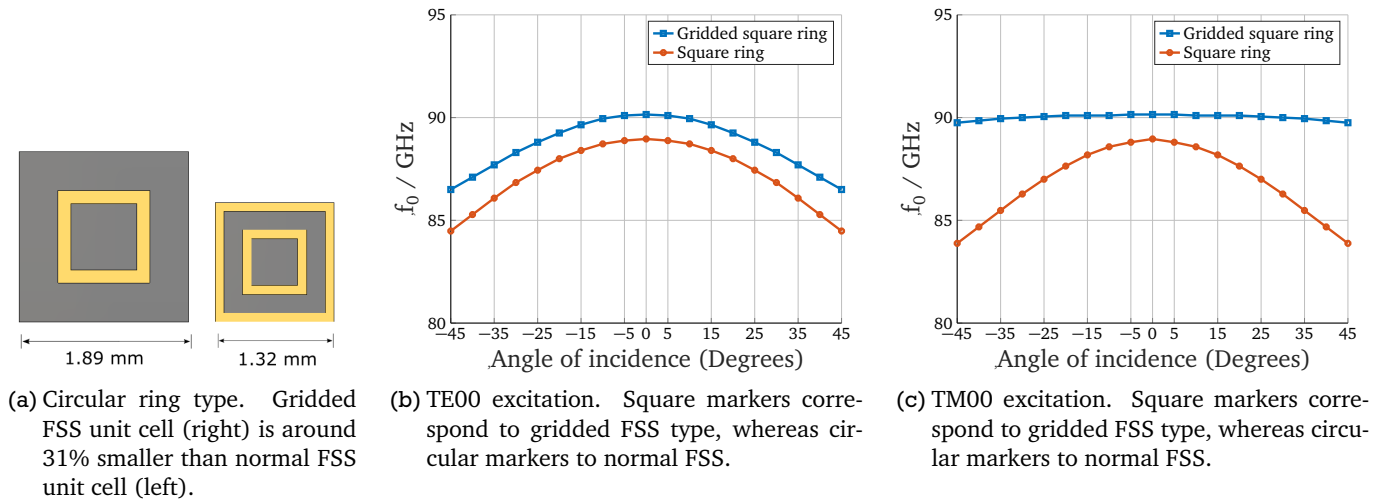


Figure 3.7: Comparison between complementary classical square ring and gridded design regarding resonance stability.

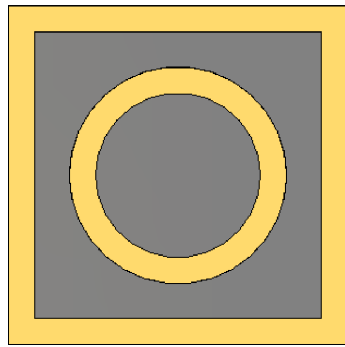
Complementary gridded circular ring FSS

The designed unit cell is displayed in 3.8 a, with its design parameters presented on table 3.2. Figure 3.8 b presents its reflection and transmission coefficient using the previously mentioned Floquet notation. Since the structure is perfectly symmetric in both axis, TE₀₀ and TM₀₀ response for frontal excitation overlap. The operating frequency of the structure is 91.5 GHz, which is measured taking into account the minimum presented in the transmission coefficient.

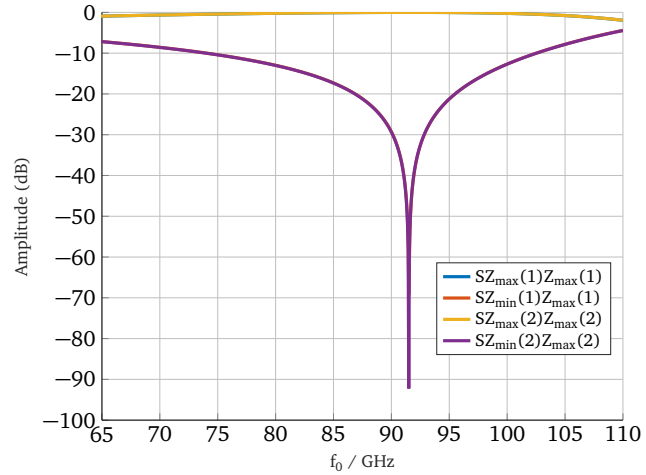
Regarding its comparison with the complementary circular ring unit cell, figure 3.9 a displays a size comparison between both of them. The gridded design is around 31% smaller than the classical one, as it is resized from an operating frequency of 75 GHz to 85 GHz for comparison purposes. Their simulated resonant frequency regarding angle of excitation for TE₀₀ and TM₀₀ polarized waves is presented in figure 3.5 b and c, respectively. The same effect regarding TE₀₀-polarized excitation is present, with similar frequency shifts for gridded and classical options of 3.82% and 4.68%. TM₀₀ excitation is completely stable for gridded design, with a 0.1% frequency shift, whereas classical unit cell has a 5.1% frequency shift.

3.2.3 Fabricated structures and characterization

In order to know the frequency response of the fabricated FSSs, their transmission parameters are measured using a 2 port configuration as depicted in figure 3.10. The set up presented is meant to measure the structure response under TE₀₀-polarized wave excitation. To measure TM₀₀ excitation, the antennas are turned 90°. The distance between FSS and each port is adjusted to 12 cm. As the antennas are too close to each other and no isolating material is used between them, an standing wave is formed from the mutual reflections between antennas and FSS under test. This resonant response is cleared using time gating

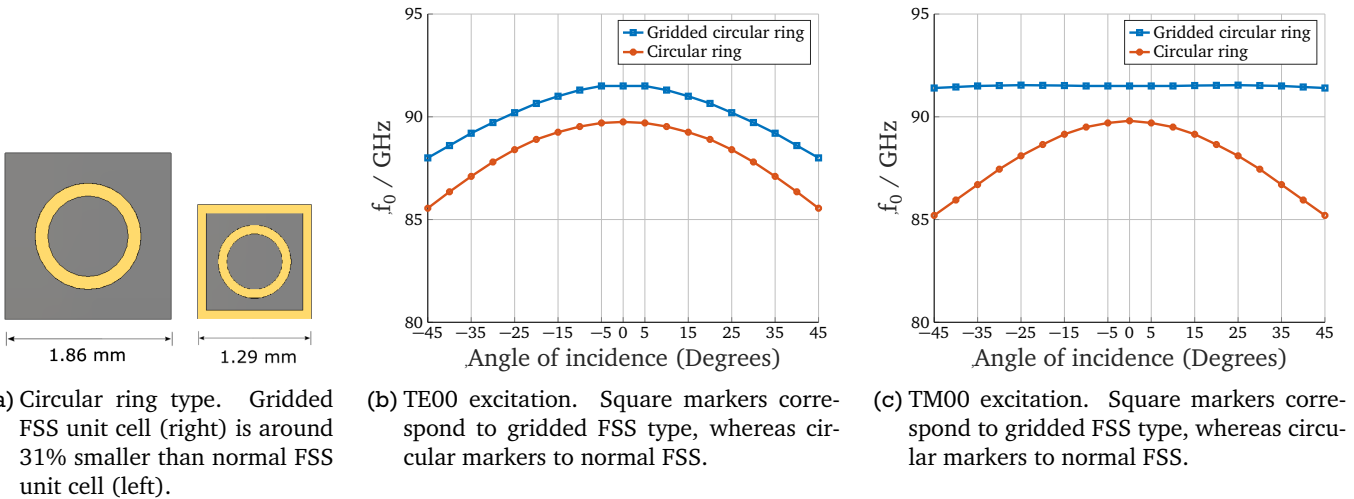


(a) Gridded circular type unit cell. PEC is represented as gray color and substrate as orange.



(b) Reflection and transmission response for both TE00 and TM00 excitations. From the graph, this structure presents passband behavior at 91.50 GHz for both polarizations. Moreover, their responses perfectly overlap for normal incidence.

Figure 3.8: Designed complementary gridded circular ring FSS and its response.



(a) Circular ring type. Gridded FSS unit cell (right) is around 31% smaller than normal FSS unit cell (left).

(b) TE00 excitation. Square markers correspond to gridded FSS type, whereas circular markers to normal FSS.

(c) TM00 excitation. Square markers correspond to gridded FSS type, whereas circular markers to normal FSS.

Figure 3.9: Comparison between complementary classical circular ring and gridded design regarding resonance stability.

between 0 ns and 1.6 ns, as explained in section 2.3. To change the angle of excitation of incoming waves, FSSs are placed on a rotary table that is controlled using a MATLAB script.

Passband designs

The fabricated passband structures are shown on figure 3.11. and their measured response on figure 3.12. An straightforward conclusion from them is the poor selectivity of these structures, since it is difficult to see a concrete operating frequency. Rather, they present huge bandwidth without significant amplitude differences in the range of 70 GHz to 80 GHz. Nevertheless, their frequency behavior resembles the simulated one, also present on the graph, but shifted 15 GHz towards lower frequencies.

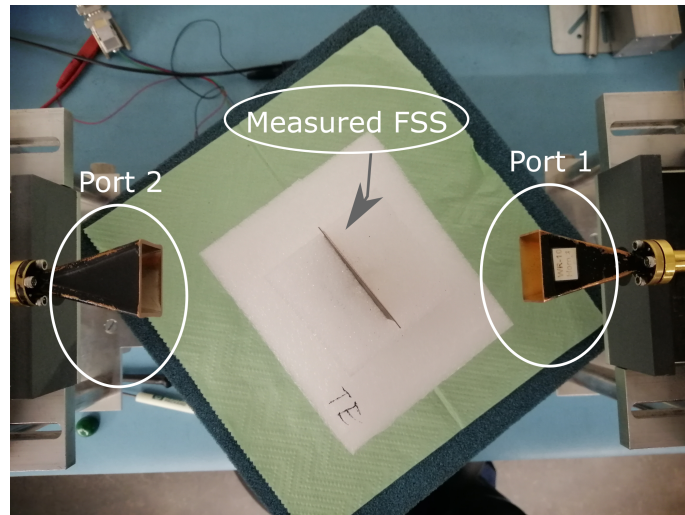


Figure 3.10: Measurement set up for characterization of FSSs

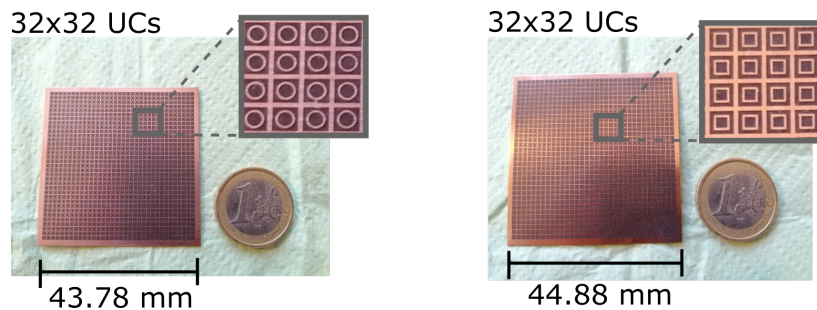
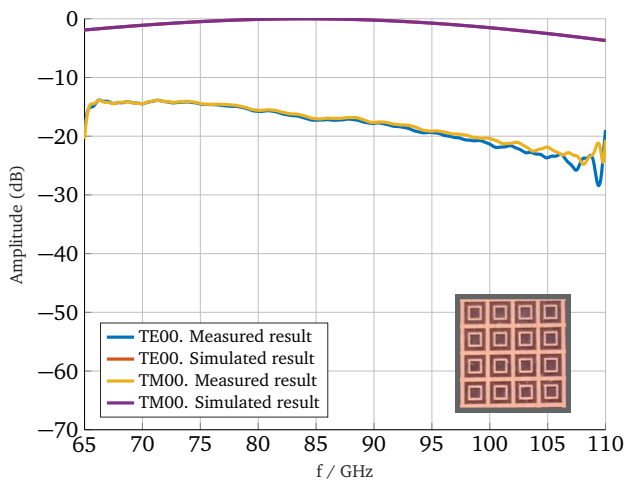
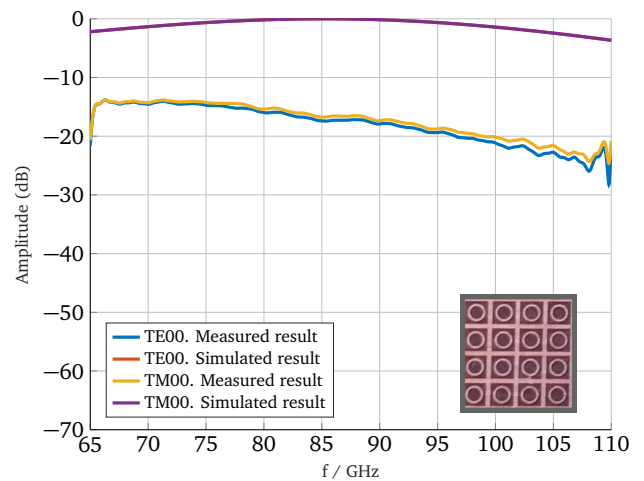


Figure 3.11: Fabricated passband FSSs



(a) Square ring design. Responses overlap due to 2-axis symmetry.



(b) Circular ring design. Responses overlap due to 2-axis symmetry.

Figure 3.12: Measured transmission coefficient for frontal incidence in passband structures.

Although the resonant frequency of such structures is difficult to determine due to their poor frequency selectivity, their behavior stability regarding angle of excitation is measured. The results are presented in figure 3.13 for both structures. The thick line represents frontal excitation, while the rest are obtained results from measurements from -45° to 45° shift. It is clear that the passband FSS behavior is very stable for both polarizations, particularly in the aforementioned frequency range between 70 GHz to 80 GHz.

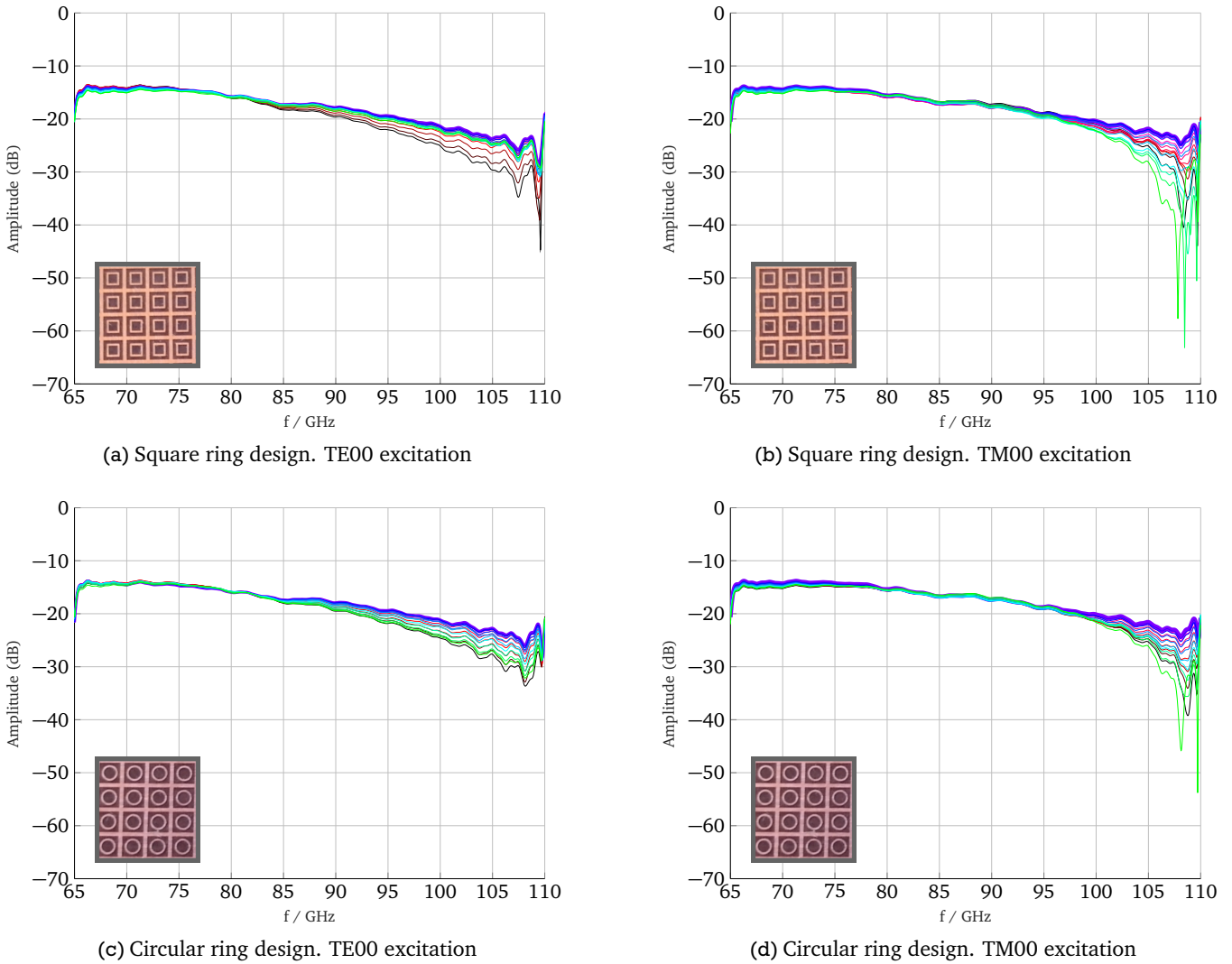


Figure 3.13: Measured transmission coefficient for angle of incidence between -45° to 45° , with 5° steps, in passband structures.

Stopband designs

The fabricated stopband structures are shown on figure 3.14. and their measured response on figure 3.15. The resonance frequency of the fabricated structures has shifted around 5 GHz towards lower frequencies regarding simulation results. This can be attributed to manufacturing tolerances. Furthermore, their frequency response for both polarizations are slightly different, owing to torsions on the FSSs, as they are fabricated using a very thin substrate. Like passband structures, they present a very low selectivity at normal incidence, which is characterized by having a wide and shallow bandwidth.

The measured transmission parameter for an angle shift between -45° and 45° is presented on figure 3.17 for both polarizations and both structures. For all the results, the resonance frequency remains inside the bandwidth of 77 GHz - 85 GHz. A comparison between simulated and measured resonance frequency regarding angle of excitation is presented on figure 3.16. First, the absence of a symmetric response regarding angle of excitation can be attributed to deformations on the FSS. Second, the resonance stability follows a similar tendency to the one predicted by the simulations, but it presents greater shifts. Table 3.3 summarizes an overview of these values.

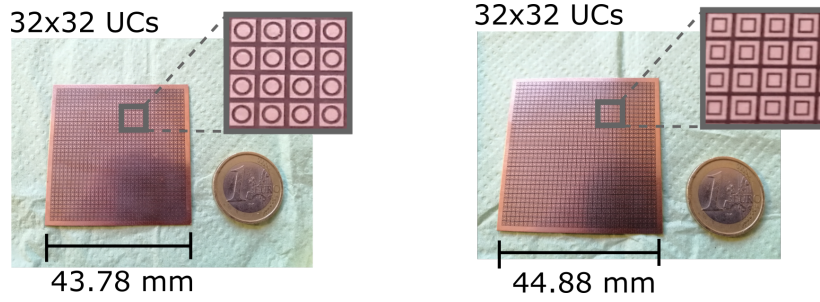
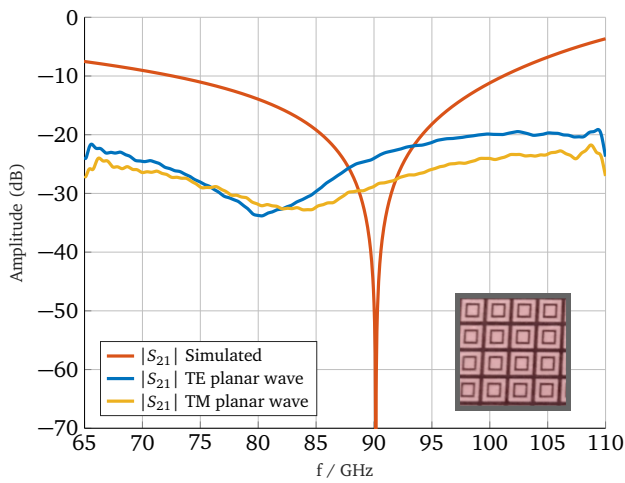
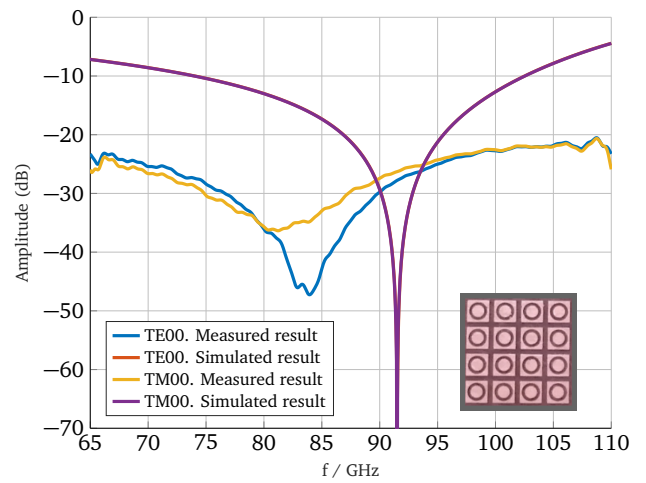


Figure 3.14: Fabricated stopband FSSs

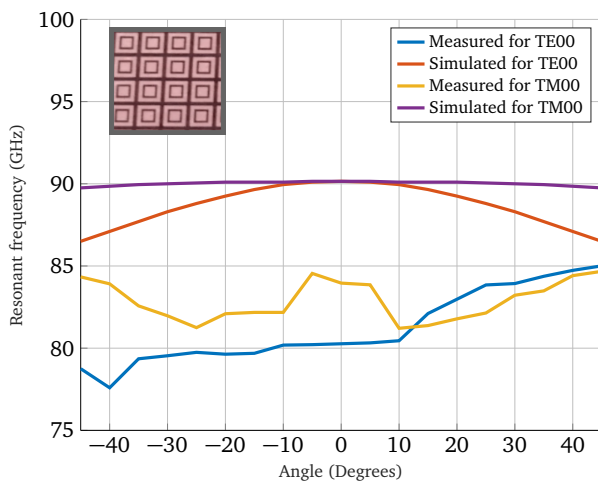


(a) Square ring design.

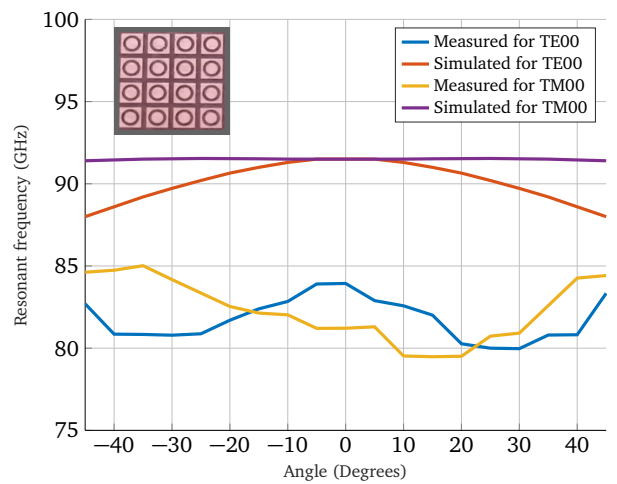


(b) Circular ring design.

Figure 3.15: Measured transmission coefficient for frontal incidence in stopband structures.



(a) Square ring design.

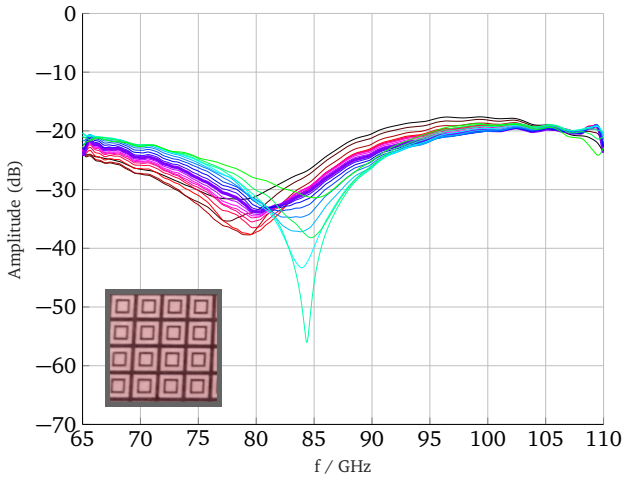


(b) Circular ring design.

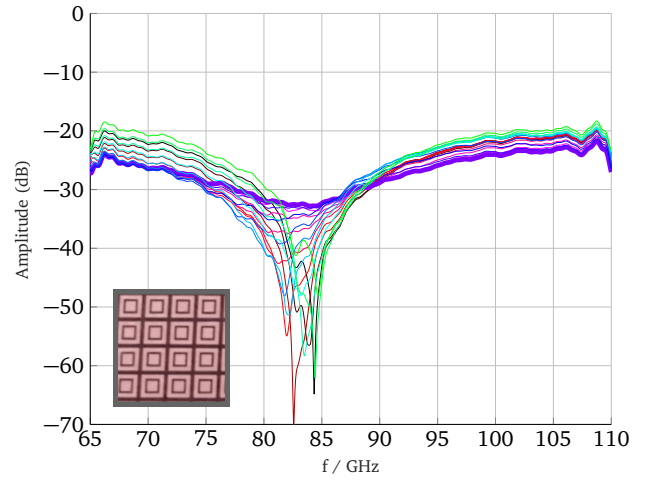
Figure 3.16: Measured resonant frequency for angle of incidence between -45° to 45° , with 5° steps, in stopband structures.

		$f_{0,Simulation}$	$\Delta f_{Simulation}$	$f_{0,Measured}$	$\Delta f_{Measured}$
Square ring	TE00	90.15 GHz	4%	80.20	5.97%
	TM00	90.15 GHz	0.44%	83.96 GHz	3.27%
Circular ring	TE00	91.50 GHz	3.82%	83.94 GHz	4.69%
	TM00	91.50 GHz	0.1%	81.21 GHz	4.67%

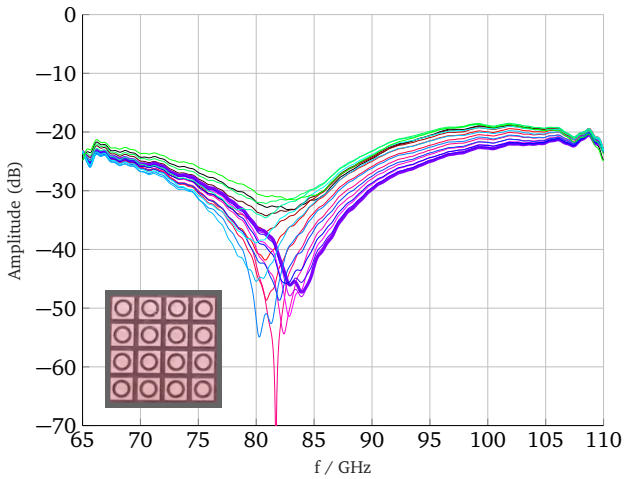
Table 3.3: Comparison between simulated and measured resonance stability.



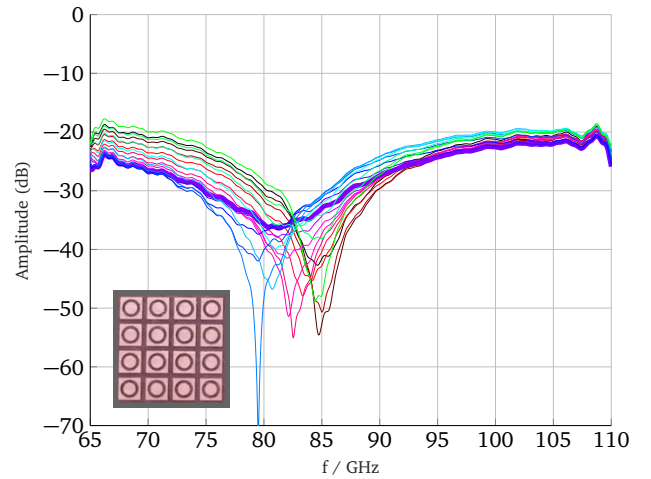
(a) Square ring design. TE00 excitation



(b) Square ring design. TM00 excitation



(c) Circular ring design. TE00 excitation



(d) Circular ring design. TM00 excitation

Figure 3.17: Measured transmission coefficient for angle of incidence between -45° to 45° , with 5° steps, in stopband structures.

3.3 Planar FSS and corner reflector

As explained in section 1.2, the combination of FSS and corner reflector allows for indoor localization. To check the suitability of the previous designs in such scenario, a corner reflector is located near the FSS, as depicted in figure 3.18, conforming the so-called "indoor tag". Moreover, only one antenna is used, to measure reflection coefficient. Finally, the distance between indoor tag and antenna is set to 40 cm, and the structure response is cleaned by using time gating between 2 ns and 5 ns.

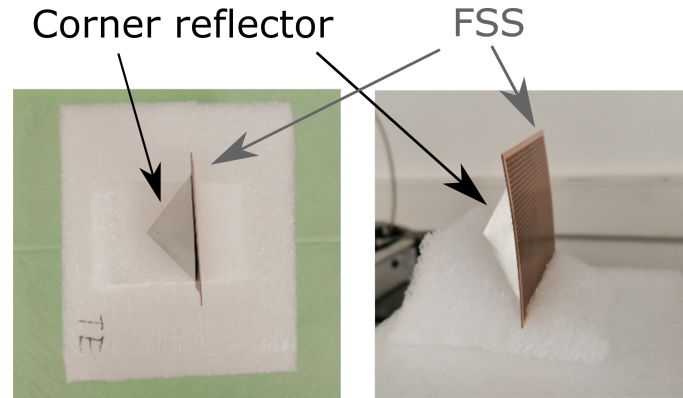


Figure 3.18: Corner reflector and FSS

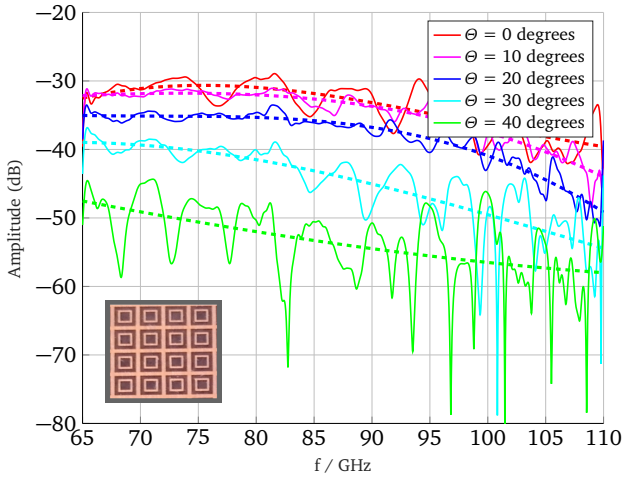
In order to further analyze the complete tag response, a 3rd grade polynomial function is used to fit the measured results. This is done owing to a standing wave between FSS and corner reflector, which introduces amplitude variations on the tag frequency response and can lead to errors while searching to its resonant frequency. By using the polynomial curve, the general tendency of tag's frequency response can be appreciated effortlessly. This curve is represented as a thick, dashed line in each graph.

3.3.1 Passband designs

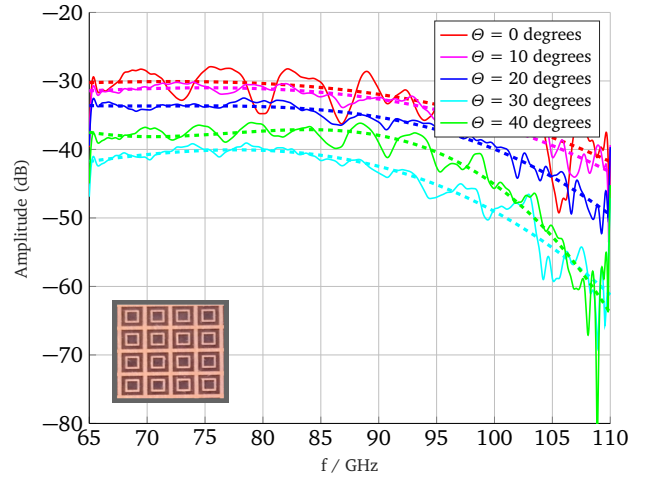
The results obtained for gridded square ring and gridded circular ring are presented in figures 3.19 and 3.20, respectively. The aforementioned standing wave between FSS and corner reflector is clearly appreciated, particularly for frontal incidence. Nevertheless, the reflection coefficient for both structures presents non-selective behavior. As expected from the designs in 3.2.1, no resonance frequency is easily found. Regardless, it is possible to appreciate frequency behavior stability. The difference between amplitudes for each angle is explained by the amount of power being reflected by the corner reflector, which decreases with increasingly angle of incidence. Since the tag is passband type, its RCS has to be computed using the amplitude of reflection coefficient in resonance. As it seems that the bandwidth is stable between 70 GHz and 80 GHz, 75 GHz is the frequency chosen to calculate the RCS of this structure, using a metal sphere with 20 mm diameter as reference and following the method explained in section 2.1. The results for both structures are presented on figure 3.21. The RCS behavior of the tag is similar as a standalone corner reflector, that presents maximum RCS for frontal incidence, which decays with increasingly angle of excitation.

3.3.2 Stopband designs

The previously characterized stopband designs in section 3.2.2 present better selective behavior than their counterparts. The results obtained for gridded square ring and gridded circular ring are presented in figures 3.22 and 3.23, respectively. For increasingly angle of excitation, a dip on tendency lines is seen, corresponding to tag operating frequency.

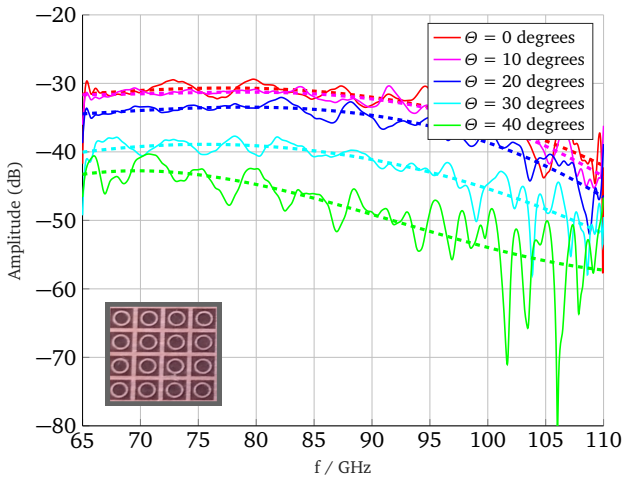


(a) Under TE00 polarized wave.

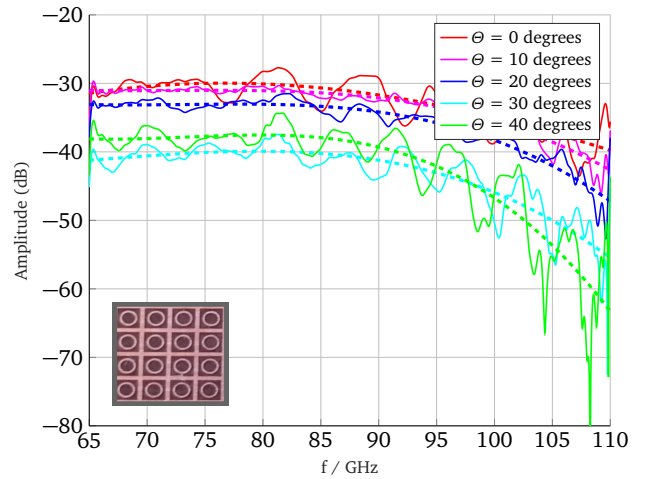


(b) Under TM00 polarized wave.

Figure 3.19: Measured reflection coefficient for passband square ring FSS with corner reflector



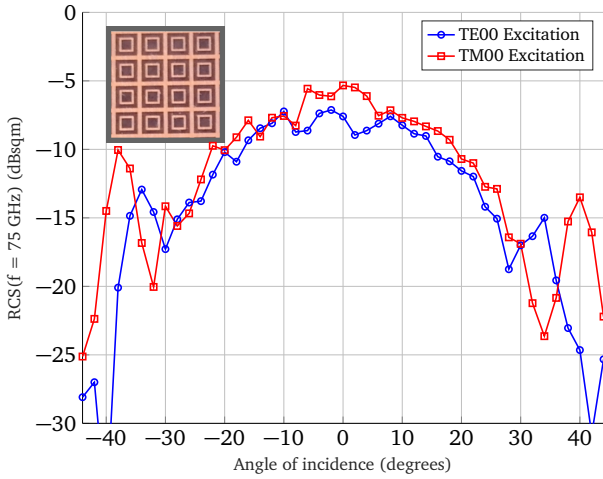
(a) Under TE00 polarized wave.



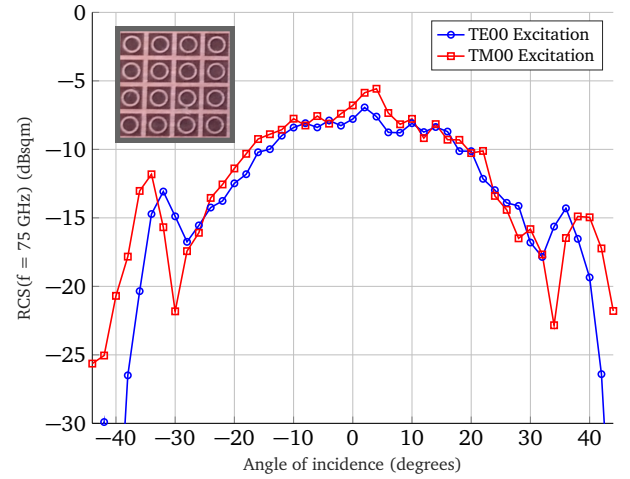
(b) Under TM00 polarized wave.

Figure 3.20: Measured reflection coefficient for passband circular ring FSS with corner reflector

In figure 3.24, the measured resonant frequency regarding angle of excitation for both stopband tags is presented. It is calculated by obtaining the frequency at which the fitted polynomial curve presents a minimum for each angle. The resonant frequency of the structure has shifted on average 2 GHz towards lower frequencies, when compared to the results presented in figure 3.16, due to coupling between FSS and corner reflector. There are three angular ranges where the tag is not working properly, corresponding to the grayed areas of the graph. Its behavior between $[-44^\circ, -40^\circ]$ and between $[40^\circ, 44^\circ]$ owes to the fact that at those angles the corner reflector does not backscatter waves, as there is too little to almost no energy coupling to it. The third region is located between $[-10^\circ, 10^\circ]$, due to the specular reflection of the structure. Since the angle of excitation is small, FSS structural reflection is also radiated towards the antenna, where it is mixed with corner reflector response. Thus, no stopband behavior is achieved. Nevertheless, both structures are stable in angles between $[-40^\circ, -10^\circ]$ and $[10^\circ, 40^\circ]$, particularly for circular ring design. Furthermore, in table 3.4, the relative resonant frequency shift that both structures present in these operating region is presented. It is calculated by subtracting the minimum frequency to the maximum frequency and then dividing the result by the average of all resonant frequencies present in the operating area. The tag that shows best behavior is the circular ring type under TM00-polarized excitation, with a relative frequency shift of 2.22%. The result can be further enhanced by decreasing the tag operating

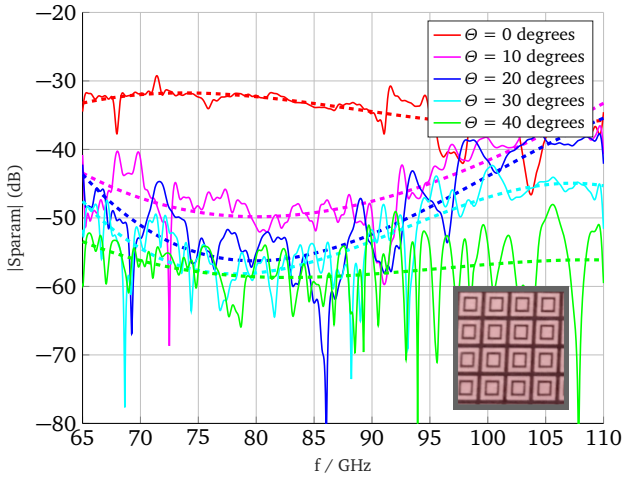


(a) Square FSS with corner reflector

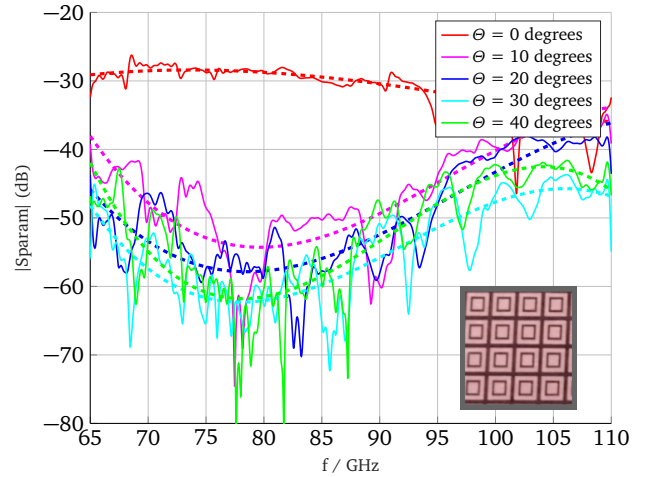


(b) Circular FSS with corner reflector

Figure 3.21: Measured RCS for passband tags at 75 GHz



(a) Under TE00 polarized wave.



(b) Under TM00 polarized wave.

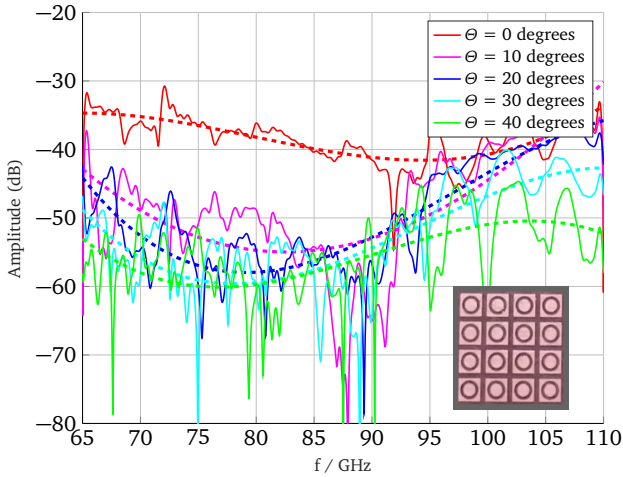
Figure 3.22: Measured reflection coefficient for stopband square ring design with corner reflector

region. For instance, when the operating region for this tag is set between $[-30^\circ, -10^\circ]$ and $[10^\circ, 30^\circ]$, its resonance shift for TE00 and TM00 excitation shrinks to 3% and 1.56%, respectively.

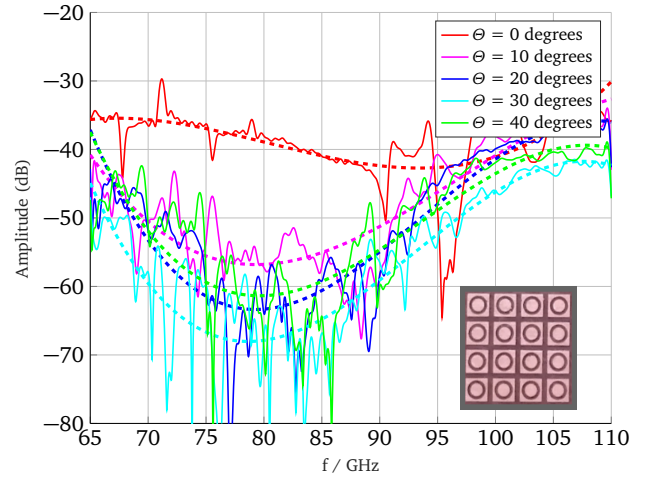
Regarding RCS, the tags are stopband type, which means that the amplitude of the reflection coefficient is low on resonance. Therefore, another frequency outside of the working bandwidth of the device needs to be chosen. In this case, 100 GHz is selected, as it is around 20 GHz higher than the tag's operating frequency. The results are presented on figure 3.25.

		f_{average}	f_{max}	f_{min}	Δf
Square ring	TE00	77.86 GHz	80.79 GHz	75.44 GHz	6.87%
	TM00	78.25 GHz	80.18 GHz	75.89 GHz	5.48%
Circular ring	TE00	78.60 GHz	80.25 GHz	75.23 GHz	6.39%
	TM00	79.29 GHz	80.42 GHz	78.66 GHz	2.22%

Table 3.4: Relative frequency shift for operating region of stopband FSS tag

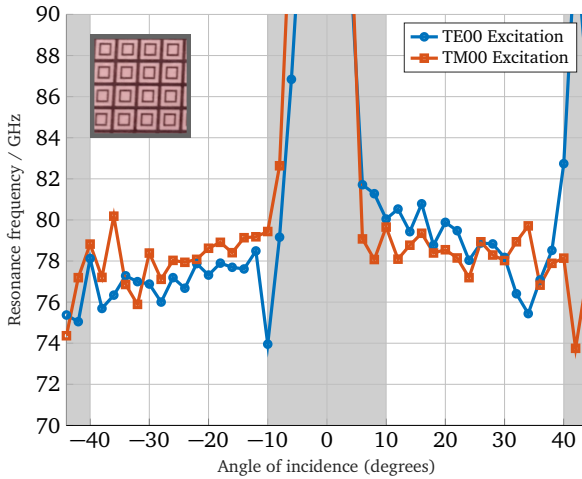


(a) Under TE00 polarized wave.

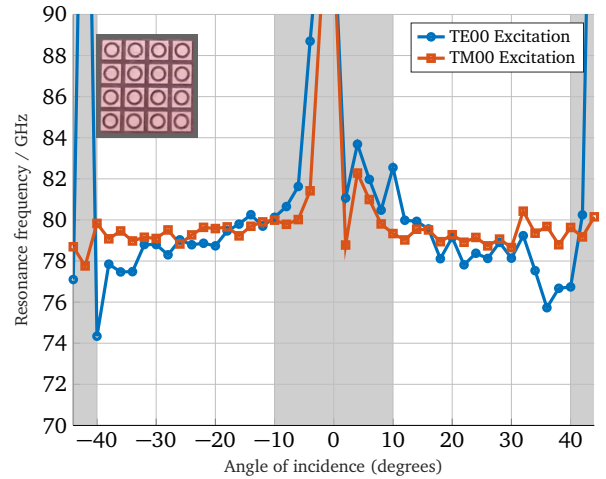


(b) Under TM00 polarized wave.

Figure 3.23: Measured reflection coefficient for stopband circular ring design with corner reflector



(a) Square ring with corner reflector



(b) Circular ring with corner reflector

Figure 3.24: Measured resonance frequency regarding angle of excitation for stopband designs

3.3.3 Discussion

During this section, passband and stopband structures applied to indoor localization have been presented. The aforementioned structures present mostly stable responses regarding angle of incidence, which shows the potential of miniaturization of unit cells to achieve resonance stability. The results obtained for whole indoor tag landmark are summarized on table 3.5

		f_0	Resonance stability	average RCS
Passband	All designs	x	No observable shift	-13 dBsqm
Stopband	Best: Circular under TM00	79.30 GHz	2.22% bandwidth	-16 dBsqm
	Worst: Square under TE00	77.86 GHz	6.87% bandwidth	

Table 3.5: Summary of results of planar FSS with CR

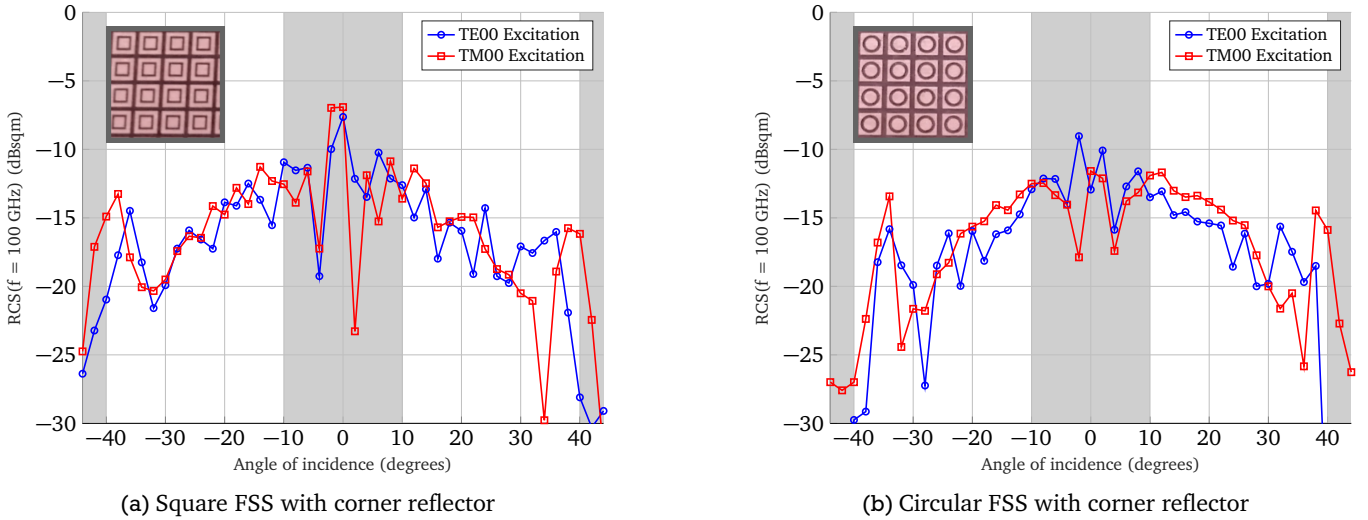


Figure 3.25: Measured RCS for stopband tags at 100 GHz

One straightforward conclusion from the results is the importance of a structure with good frequency selective behavior, meaning that they present deep and thin operating bandwidths. On the one hand, this is not the case with the measured passband structures, since it is not possible to obtain their concrete resonant frequency. On the other hand, the stopband structures present better frequency selectivity than their counterparts. Thus, it is easier to detect their operating frequencies. Regardless, the higher the selectivity that a structure presents, the better and easier that its resonance frequency is detected. Therefore, one possibility to enhance the results would be to invert the designs and its frequency behavior. The passband structures by themselves already present high transmission coefficient, as the incoming wave mostly impinges on a low ϵ_r substrate. Therefore, stopband behavior is more suitable for these structures. The same effect happens for the designed stopband FSSs. As they are mostly made of metal, they naturally present an already high reflection coefficient, which explains the low amplitude difference between their resonance frequency and the rest of the spectrum. Thus, they are better suited to work as passband structures. In figure 3.26, this concept is shown by comparing Floquet results of designed complementary gridded square FSS (blue) and a classical slot based cross-dipole FSS (orange) such as the one presented on figure 2.3b. While the cross-dipole presents a clear passband response, the gridded square FSS shows significantly worse frequency selectivity owing to being stopband. Further possibilities to design FSSs with proper resonances would be to use fractal unit cells such as the one presented on [29], as they are also miniaturized FSSs.

A second conclusion is that the structures present good range to work in indoor environments, once their selectivity limitations are solved, owing to their monostatic RCS value. Following the results presented in [11], such RCS value means a readout range that extends up to three meters.

Finally, the limitations of using corner reflector in combination of FSSs as tag landmarks have been addressed. Mostly, there are several angular ranges for which this approach does not work properly, either due to the combination of FSS' specular reflection and corner reflector response on the antenna, or because the corner reflector is not working properly anymore. Furthermore, frequency shift presented by indoor tag can be decreased by selecting an appropriate angular operating region. On the one hand, this results in less bandwidth needed per tag. On the other hand, more tag landmarks are needed to cover the same indoor area. The most stable tag (circular ring FSS under planar TM-polarized wave) presents a moving resonance in a bandwidth of 1 GHz for incoming waves with angles between 10° and 40° . This means, that around 40 of these tags could be used in W-band (65 GHz to 110 GHz), once its low selectivity limitations are solved.

The designed structures aim to improve the indoor tag landmark presented in [11], by introducing the concept of orientation insensitive FSSs. In that work, cross-dipoles are used as FSS' elements. Moreover, it shows good resonance stability for TE00 excitation, defined as E plane, and the opposite for TM00 excitation.

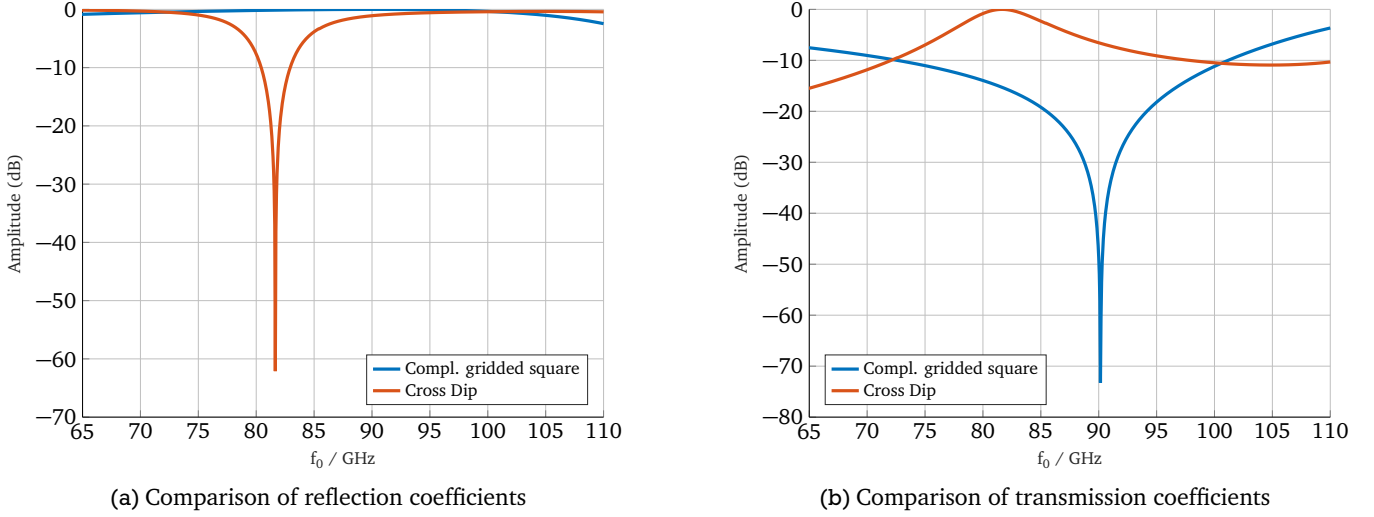


Figure 3.26: Comparison between complementary gridded square FSS and classical cross-dipole FSS

	Reference [11]		This work	
	TE00	TM00	TE00	TM00
Unit cell	Cross-dipole		Gridded circular ring	
Response	Stopband		Stopband	
f_0 (GHz)	78	78	78.60	79.30
Operating range	$\pm 36^\circ$	$\pm 24^\circ$	$\pm 40^\circ$	$\pm 40^\circ$
Δf	1 %	3.84 %	2.22 %	6.39 %
RCS (dBsqm)	0...-30	0...-30	0...-30	0...-30
N_{tags} assuming $\pm 40^\circ$	8	x	32	8
Bits assuming $\pm 40^\circ$	3	x	5	3

Table 3.6: Comparison between indoor tag landmarks of this work and [11]

A comparison between this paper and the presented complementary gridded circular FSS is displayed in table 3.6. In the comparison, the amount of tags that can be used in W-band is adjusted to represent a natural number of bits. From the results, the cross-dipole FSS presents better resonances stability in limited angular range. However, when considering an operating range of $\pm 40^\circ$, the designed gridded circular ring FSS improves the available bits usable on W-band for both polarizations. In the case of TE00, it is increased from 3 bits to 5 bits. For TM00, cross-dipole FSS resonances lie outside W-band and thus are not considered. However, this is not the case for designed FSS, which allows 3 bits in this polarization. In light of the above, the indoor tag landmark that uses complementary gridded circular ring FSS is improved regarding angular operating range and achievable number of bits.

4 Spherical FSS

By using 2D FSS, nearly orientation-insensitive resonance frequencies can be achieved for a wide angular range of incoming waves. However, they present increasingly narrow resonances and other bandwidth instabilities with increasing incident angles. One possibility to bypass these limitations is inspired on the isotropic behavior of metallic spheres, whose reflection coefficient is always the same independently of angle of arrival of interrogating signal. Therefore, using spherical surfaces as a base, an FSS whose response is always the same independently of angle of excitation can be designed. In layman terms, *the FSS must look the same from all angles* to achieve orientation insensitivity.

This chapter introduces how to design and generate the aforementioned structures in CST studio, as well as presents designs based in the premise of combining a spherical FSS and a spherical retroreflector.

4.1 Design challenges in spherical FSSs

Planar 2D FSS are easy to design and fast to simulate because they present periodicity and can be considered as infinite surfaces, which reduces the computation to only one unit cell of the whole structure. However, this is not the case for spherical FSS. Even if they present a perfectly symmetrical structure, the incoming planar wave arrives to each element of the FSS with a different phase, which means that the structure can not be considered as periodic. Therefore, full wave simulations are needed to understand the behavior of such devices. However, these structures are usually one or several orders of magnitude larger than operating wavelength, which results in long simulation times. Currently, there is research aimed to achieve their fast simulation by using method of moments (MoM) combined with full wave analysis [37] [38]. Nevertheless, their implementation lies outside of the scope of this work, in which only full wave simulations by means of CST Microwave Studio are carried out.

The response of spherical FSSs is highly dependent on all design variables of the structure, such as radius, type of unit cell used, separation between unit cells and element distribution. As each element is excited with a different phase, their resonant frequencies differ. This can be partially solved by using unit cells that are relatively insensitive to excitation angle, such as circular rings, or increasing the radius of the structure. For large radii, the section of surface illuminated by the incoming excitation can be approximated to be planar. Even in these cases, spherical FSS behavior is not the same as its planar equivalent, since a slight curvature affects its response. Moreover, depending on element arrangement the inter-element coupling can be asymmetrical, which further modifies FSS behavior. As an example, in FSS presented in [38], three different resonance frequencies arise when increasing the number of elements present on the curved surface, whereas the planar equivalent has only one well-defined resonance. Regardless, curved FSSs with clear passband response have been achieved at around 10 GHz in [39] by etching a certain number of elements in a relatively small spherical cap. Their results are displayed on figure 4.1.

For small radii, coupling effects usually result in a shift in operating frequency regarding the planar FSS and a dampen of the transmission or reflection coefficient. Moreover, for large curved structures wide bandwidths arise, as a result of the different resonant frequencies of the FSS's elements. Regardless, in order to characterize and design these structures, full wave electromagnetic simulations need to be carried out. Since a spherical FSS can have up to hundreds of elements etched on its surface, a combination between MATLAB and CST Microwave Studio has been done to be able to generate the necessary simulations and obtain the designed structures frequency response, as explained in subsection 4.1.1.

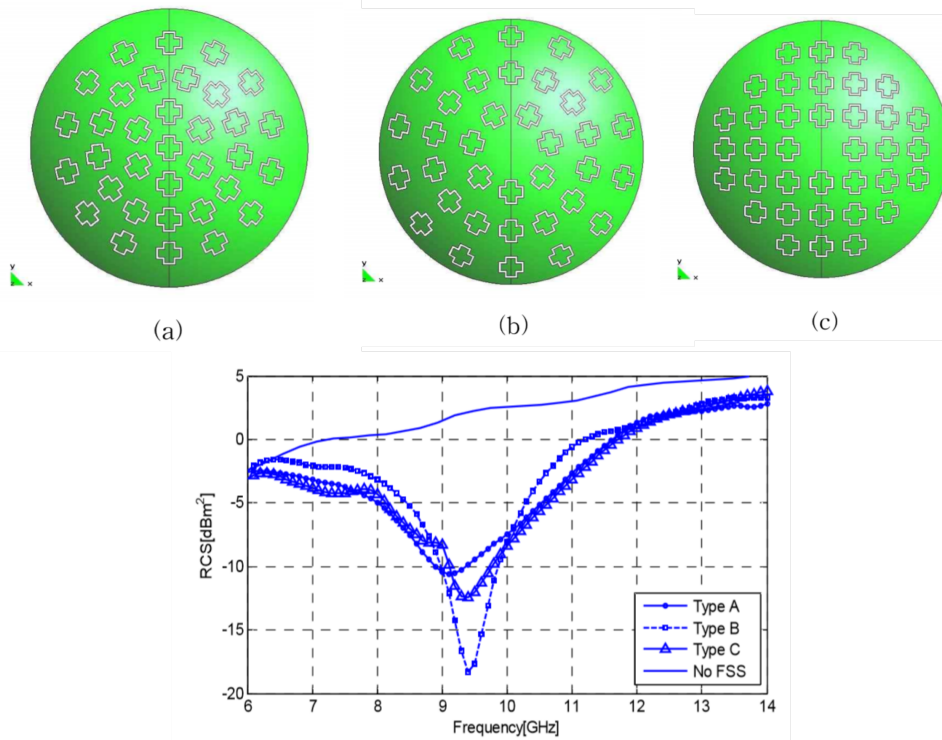
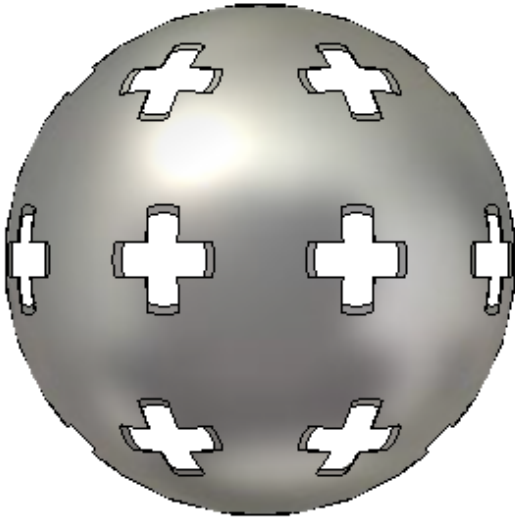


Figure 4.1: Passband spherical FSS [39]

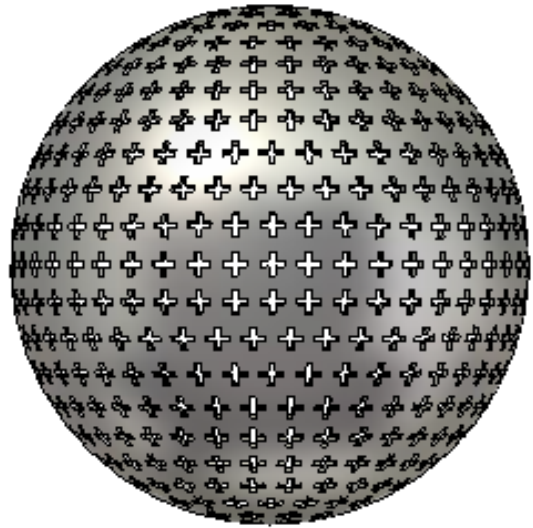
4.1.1 Generation of complex structures with MATLAB and CST Studio Suite

CST Microwave Studio is a full wave electromagnetic simulator that is widely used in microwave design. Although its modeling tools are very potent, there are specific structures whose manual generation takes too long. For instance, consider the structures present in figure 4.2a and b. The left model is quite simple and fast to generate manually, provided that the rotations needed for each element are already calculated. However, that is not the case for the big spherical FSS shown in the right side. The sheer complexity that it presents complicates its generation in a reasonable time span. Moreover, when changing design parameters such as elements' positions, the whole process would need to start again, since manual creation on CST relies on "repetition" value. This value varies from one circle to another of different size, if angular distance between elements is kept constant. Thus, it would need to be calculated again. However, that is not the case when automatizing the generation of structure because only basic parameters need to be configured. Thus, generation of similar structures but with changed parameters is more robust, as positions and rotations are calculated from scratch every time the script is executed. Therefore, in this work the generation of such structures is automatized by using scripts in software MATLAB.

CST simulations are generated by compiling a "history list" that is written in VBA basic code. Moreover, in Windows it is possible to send own made instructions to this list by using a serial connection between CST and activeX server. Therefore, the hard task of generating VBA code for the simulation can be done automatically in a outside program and then send it to CST to be compiled. MATLAB already implements several user-made toolboxes with the capability to control CST's history list. In this work, [40] and several self-made functions, provided in appendix A, are used to generate the structures. The general process to generate complex spherical FSS is displayed in figure 4.3.



(a) Small spherical FSS, with known element positions, it is easy to create each element individually and then rotate it to its position.



(b) Big spherical FSS. Although its possible to create it manually using "translate" and "copy" operations, using MATLAB it was generated in around 5 mins.

Figure 4.2: Example of two spherical FSS

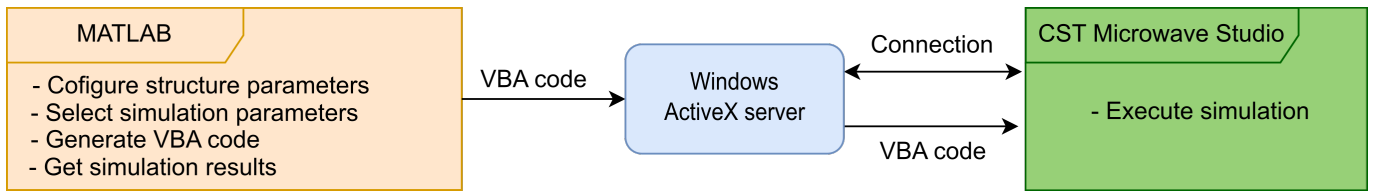


Figure 4.3: Sketch of connection between MATLAB and CST

MATLAB and CST in this work

The flowchart of the developed code is displayed in figure 4.4. First, structure and simulation parameters are selected. Then element positions on sphere surface according to a pre-defined pattern are calculated. Afterwards, the rotation needed to drive those elements to these positions are computed. Finally, VBA code to generate the structure is sent to CST and specific simulation parameters are also modified.

The pattern in which the FSS elements are arranged on its surface is critical in the structure behavior. In this work, two patterns with different purposes are used. The first one aims to maintain an equal distance between FSS elements by profiting from the so-called Archimedean solids, whereas the second one aims to fit a natural number of elements within the sphere, by modifying inter-element separation.

Archimedean solids are the only thirteen convex uniform polyhedra composed of two or more regular polygons meeting in identical vertices. As they are formed by regular polygons, the distance between vertices is exactly the same. Moreover, it is possible to re-dimension this distance so all vertices lie within a certain sphere surface. This is used to map planar 2D FSS to that sphere, by locating FSS' elements at vertices' coordinates. However, they have the disadvantage that their vertex number is low, which means that there are areas of the sphere without any element present. This was solved by calculating the centroid coordinates for each polygon, and adding a new element position there. A further solution would be the use of Goldberg polyhedra. The main solid used in this work is the so-called "Bucky ball" or football, which is comprised of regular hexagons and pentagons. Figure 4.5 a shows MATLAB result of a generated FSS using this pattern and cross-dipole elements.

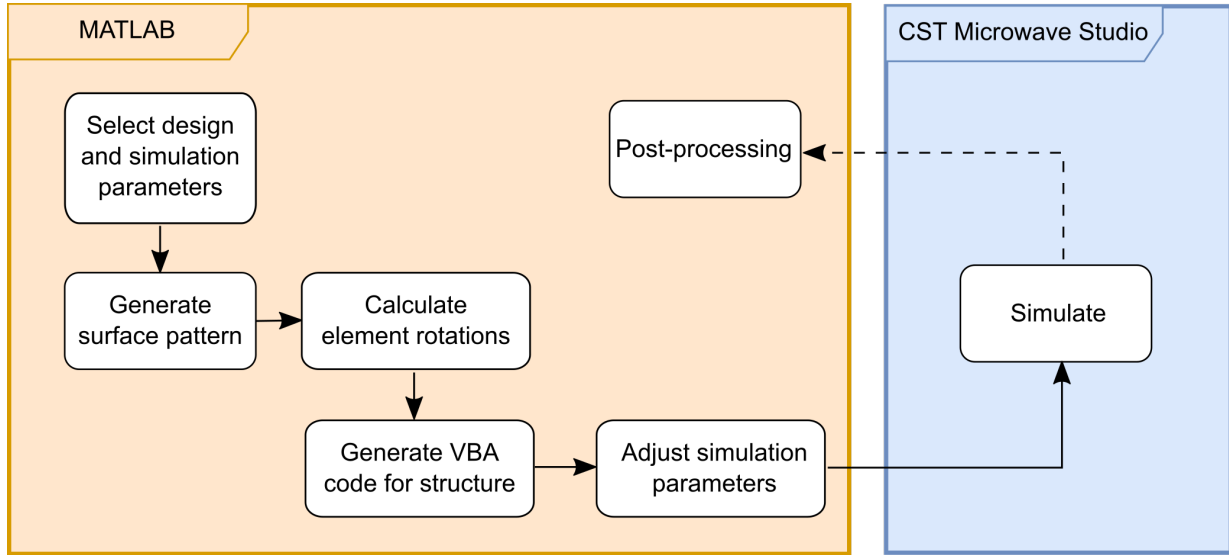


Figure 4.4: Flowchart of the process to generate spherical FSS

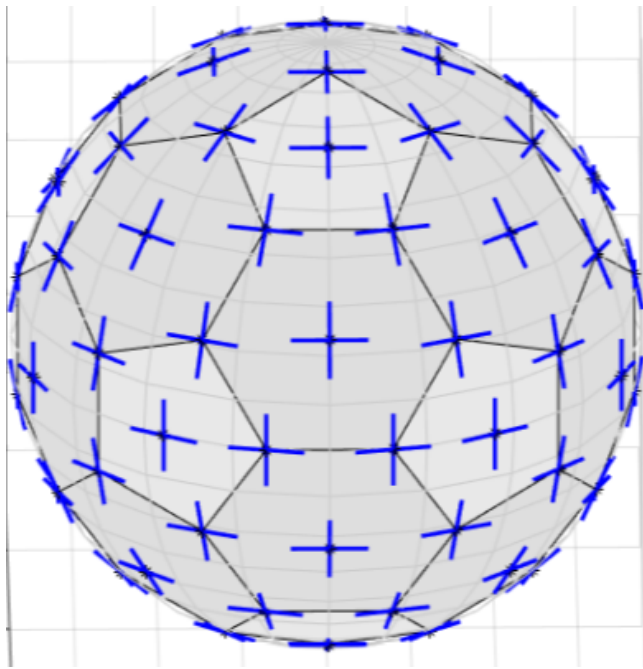
The previous approach has the disadvantage that vertices' positions are fixed, which means that, for increasingly large sphere's diameters, distance between elements is larger. Since the response of FSS is dependent on that distance, element's separation needs to be scaled with sphere's diameter. To be able to independently decide resonance frequency and diameter, a custom algorithm is implemented. It works by dividing the sphere in a natural number of parallel cutting planes. The intersection between them and the sphere generates circles, in which element positions are distributed evenly, trying to achieve a separation as near as possible to the designed unit cell size. The main purpose of this algorithm is to fit an exact number of unit cells within the sphere independently of its diameter, which means that separation between elements is usually not conserved. Appendix C shows the code implemented to achieve this pattern. Figure 4.5 b shows MATLAB result of a generated FSS using this pattern and cross-dipole elements. It is seen that element positions are more regular compared to bucky pattern displayed in Figure 4.5 a.

In CST, elements first need to be created and then rotated to their positions. In 3D coordinate systems, it is possible to bring an object from one position to another by rotating it around two reference axis (X,Y,Z). MATLAB and CST both use right-handed coordinate systems, but with different axis orientation. Therefore, the computation of proper angular rotations is a complex task. In this work, FSS elements are generated in CST at $(x,y,z) = (0, \text{sphere_radius}, 0)$ and rotated α and β degrees around Y and Z axis, respectively. However, when calculating their rotating angles in MATLAB, original element location is set to $(x,y,z) = (0,0,1)$, due to the coordinate system mismatch between both programs. Considering \vec{A} as unity vector between point of creation of element $(0,0,1)$ and sphere center and \vec{b} as unity vector between desired position and sphere center, α and β can be calculated as

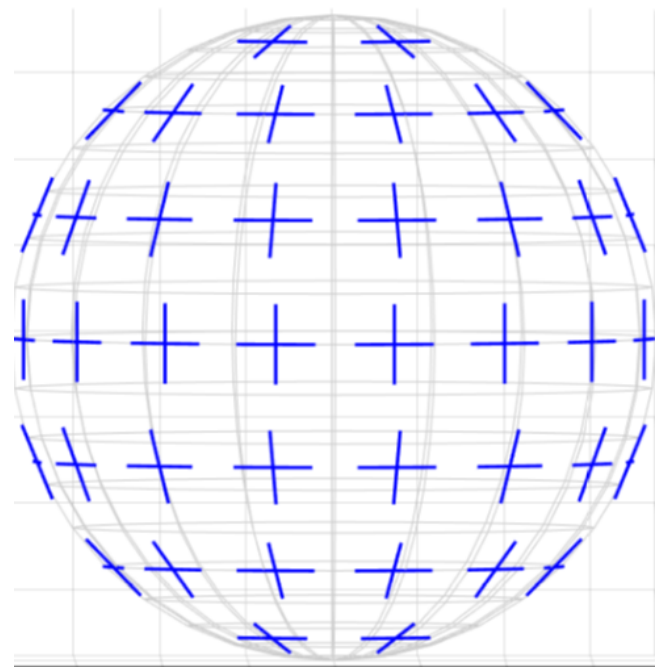
$$\alpha = \text{acos}(\vec{A} \cdot \vec{b}) \quad (4.1)$$

$$\beta = \text{atan2}(\vec{b}(2), \vec{b}(1)) \quad (4.2)$$

Once these angles are calculated, FSS elements can be created from MATLAB in CST. Annex B shows two examples about how to do this using cross-dipole and tripole elements. Once all of the structure is created, two final rotations of -90° around X and Y axis achieve coordinate system conformity, meaning that the pattern designed in MATLAB is exactly reproduced in CST. As an example, the CST equivalent structures to MATLAB plots of Figure 4.5 is displayed in Figure 4.6

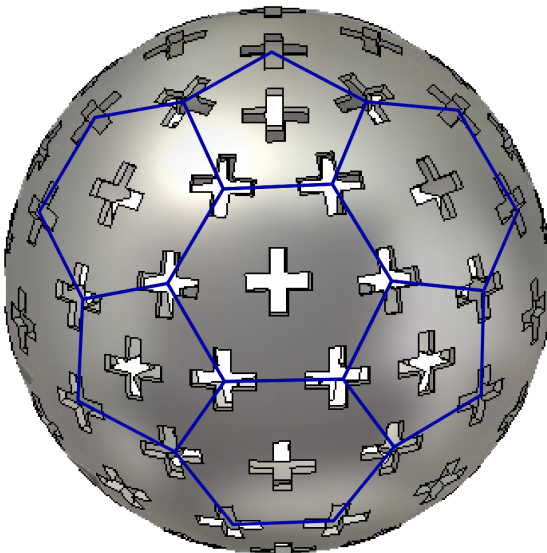


(a) Using bucky ball pattern. The original planar design has an element separation of 2.74 mm. However, due to archimedean solids' vertices having fixed positions, this distance is increased to 3.077 mm.

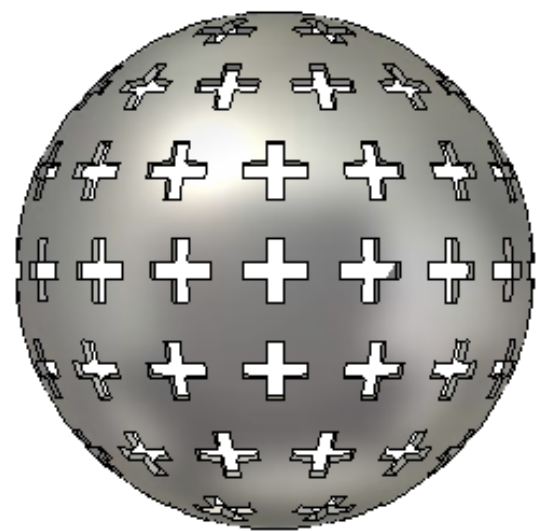


(b) Using custom designed pattern. In this case, element separation is variable but averages 2.88 mm, which is closer to original value of 2.74 mm than bucky ball option.

Figure 4.5: MATLAB output of spherical FSSs with 15mm diameter using different element patterns.



(a) Using bucky ball pattern.



(b) Using custom designed pattern.

Figure 4.6: CST output of spherical FSSs with 15mm diameter using different element patterns.

After creating the structure, simulation settings need to be adjusted. This is due to wanting planar wave excitation. Usually, simulations in CST are done by using waveguide ports and creating planar wave conditions by using electric and magnetic boundaries. This creates sort of "closed box" simulation environment. However, in this case the reflections between structure and exciting signals are also reflected in boundaries, creating a highly resonant and complex environment, whose response is completely different from reality.

A solution would be to use open boundaries. However, the wave excited by waveguide ports in these conditions is not planar, which changes FSS behavior. Therefore, the chosen approach is to use planar wave excitation, and work using field monitors to get spherical FSS frequency response, by computing its RCS at the frequency they have been set to. Thus, a decent amount of field monitors are needed to get enough frequency resolution. After simulation, their mono static RCS responses are obtained in post processing step using getField function already implemented in [40], by using

$$RCS_{\text{mono}} = RCS_{\text{bistatic}}(\theta = 0, \varphi = 0) \quad (4.3)$$

The previous equation accounts for the transmission coefficient of the structures. Since CST calculates the Bistatic RCS, the transmission can be obtained as

$$TX = RCS_{\text{bistatic}}(\theta = 180, \varphi = 0) \quad (4.4)$$

4.2 Indoor tag landmark with spherical FSS and retroreflector

A passive indoor tag landmark is formed by combining retroreflectors and FSSs. In section 3.3.3, limitations of planar FSSs with corner reflectors are addressed. Two of the most important drawbacks are instability of frequency behavior with different angle of excitation and the impossibility of correct identification of resonance frequency in frontal incidence.

The use of lens-based retroreflectors instead of corner reflectors combined with spherical FSSs could be used as a potential solution to bypass both limitations. When a passband FSS is used, its working frequency should be the only one that couples inside the lens. Thus, the amplitude of backscattered wave at that frequency is Δ_{RCS} dB higher regarding the rest of spectrum. The opposite happens for stopband FSSs. The reflection coefficient is boosted in whole spectrum but the FSS' working frequency. Furthermore, an ideal spherical FSS has isotropic response, which solves the problem of resonance instability regarding oblique incidence of interrogating signal.

A lens-based retroreflector is made by enclosing the backside of a lens, for instance a Luneburg lens, with a metallic semi sphere. When integrating lens and FSS, two options are to manually paste the FSS elements on the uncovered lens surface, thus rendering it unusable for future applications, or fabricating the FSS in a low ϵ_r substrate. In both cases, misalignment of elements is a concerning matter. On the one hand, manual placement requires precision difficult to achieve at mm-wavelengths. On the other hand, the planar substrate needs to be bended to spherical form, which introduces rugged borders and inequalities along the whole FSS. As a consequence, an FSS consisting of slots etched on a metallic semi sphere is used, in order to finish encasing the whole lens in metal. It can be fabricated directly by milling the elements in a metallic semi sphere or printing it using metal-based 3D printing technologies. When metal semi sphere and spherical FSS are fabricated so they perfectly enclose the lens, they can be pasted together *from the outside* using materials such as adhesive copper, thus not affecting the lens at all. This allows for further testing and prototyping using the same lens, that is usually the most expensive part of such tags.

Slot-based FSS have usually bandpass response, as presented in section 2.4. In figure 4.7, the working principle of an indoor tag landmark using lens-based retroreflector and bandpass FSS is presented. As aforementioned, only the operating frequency of the FSS, represented by orange line, propagates through FSS into the lens. Afterwards, it is focused on the lens' focal point and backscattered towards the reader by the metallic semi sphere. This reflection results in Δ_{RCS} dB higher RCS. The response of such system is also presented on the same figure, with operating frequency of FSS standing out regarding rest of spectrum. When the lens presents sufficiently high Q factor, the backscattered response of the rest of spectrum can be taken out, thus enabling easy detection of f_0 at receiver by searching for maximum amplitude in reflection coefficient S_{11} .

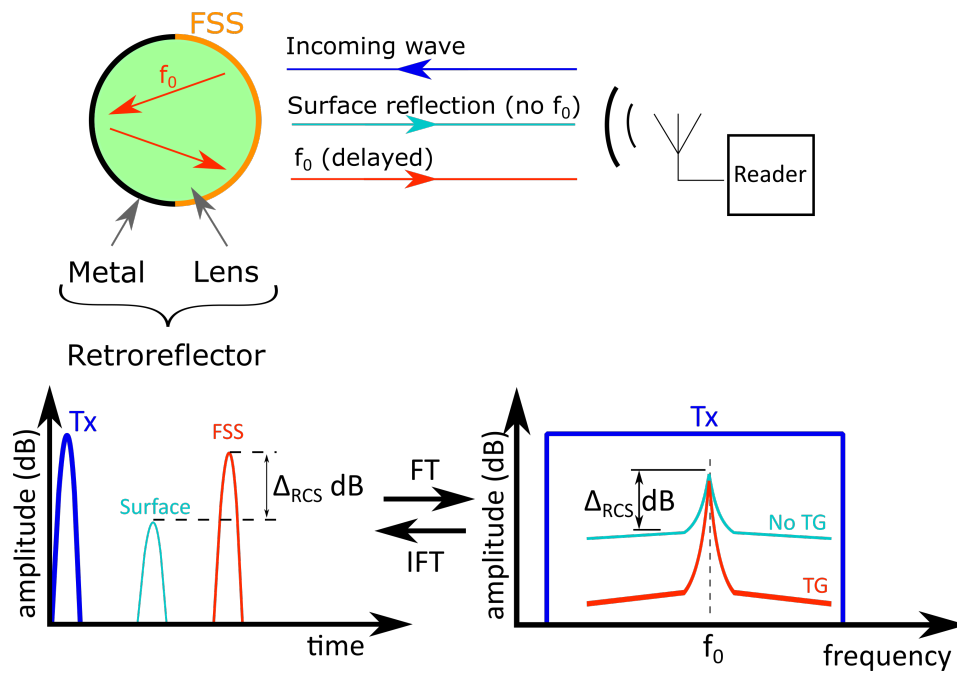


Figure 4.7: Working principle of spherical tag landmark. Incoming wave (dark blue) is reflected first without f_0 (light blue) and then boosted f_0 (orange) is backscattered with a delay. The frequency plot represents reflection coefficient. Without time gating (light blue), f_0 is mixed with backscattered wave, but still stands out. With time gating that encloses the orange pulse, only f_0 remains on reflection coefficient.

4.2.1 Designed FSSs

To fabricate slot-based FSSs, two technologies are considered, mainly milling and metallic 3D printing. The first one needs five-axis milling machines, due to the structures' complexity, which increases final cost. Moreover, the minimum feature size required to fabricate such structures at 85 GHz was found to be bigger than the tolerances achievable by several consulted milling companies. Therefore, the latter technology is chosen to fabricate spherical FSSs, as it is cheap and allows for flexibility while designing. However, there are design constraints that need to be taken into account. First, the minimum feature size achievable by metallic 3D-printing is 500 micrometer (μm) [41] [42] [43]. Second, resonance-stable structures like the ones presented in chapter 3 are not possible to be implemented, as they need to be placed on a substrate to maintain structural integrity. Therefore, only simple elements that could be milled in a metallic surface such as slots-based elements like dipoles or tripoles are considered when designing the FSS. This is because the process of milling and 3D printing are analogous but complementary. While the first one etches FSS' elements on the sphere by retiring metal, the latter creates the structure from scratch, taking into account where material should - and should not - be placed.

Following the working principle presented in figure 4.7, two metallic FSS are designed to fit two available Luneberg lenses with diameters of 15 mm and 20 mm. The first one has element distribution following "bucky ball" pattern presented in section 4.1.1. The second one uses custom pattern that is also explained in that section. Moreover, the elements chosen to create the FSS are cross-dipoles, whose minimum feature size must be 500 μm . First, two planar FSS are designed to work around 85 GHz, one for each pattern. The design parameters of both are presented in table 4.1. Their ideal, simulated response is displayed in figure 4.8. Their behavior is passband at their operating frequency, as explained in section 2.4. A relevant limitation of the unit cells is their relatively high transmission coefficient after resonance frequency. Instead of decaying, it stabilizes at -10 dB, owing to the relatively large slot width. Their size, 0.5 mm, is around $\lambda_0/6$ for 95 GHz ($\lambda_0 = 3.16$ mm). Thus, the designed cross dipole is not able to completely inhibit wave propagation after that frequency. When element width is decreased to 0.15 mm ($\lambda_{0,95\text{GHz}}/20$), its trans-

mission coefficient at higher frequencies decreases to -20 dB. Regardless, as aforementioned the minimum feature size achievable by 3D printing is 0.5 mm.

Pattern	Bucky ball	Custom
Lens diameter (mm)	15	20
Element length, l (mm)	1.85	1.87
Element width, w (mm)	0.5	0.5
Element separation, p (mm)	3.027	Variable. 2.88 on average.
Metal thickness, w (mm)	0.75	0.75
f_0 (GHz)	84.53	84.31

Table 4.1: Design parameters for the two cross-dipole spherical FSSs

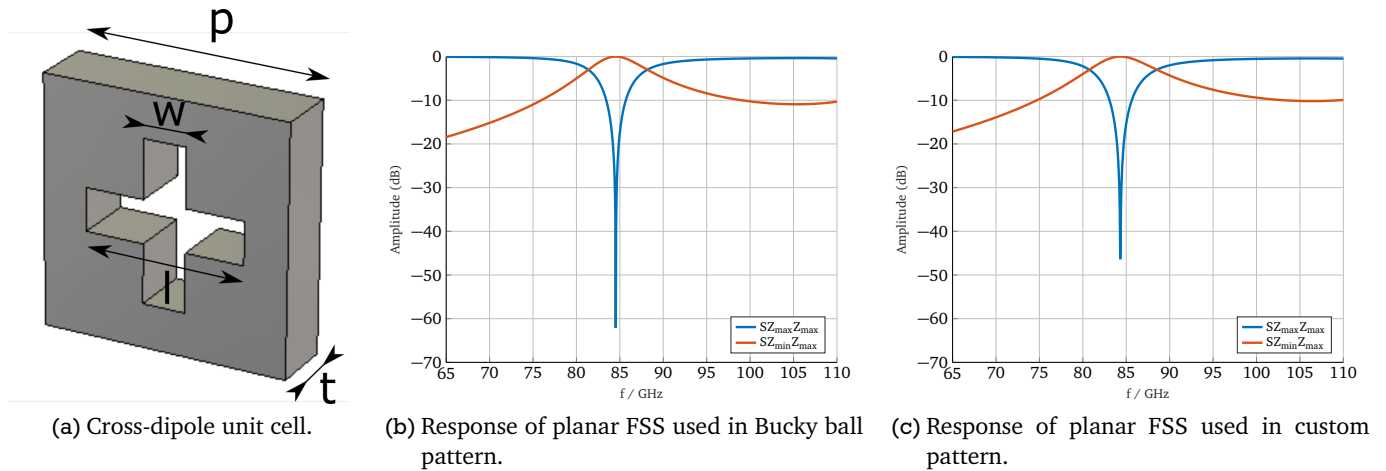


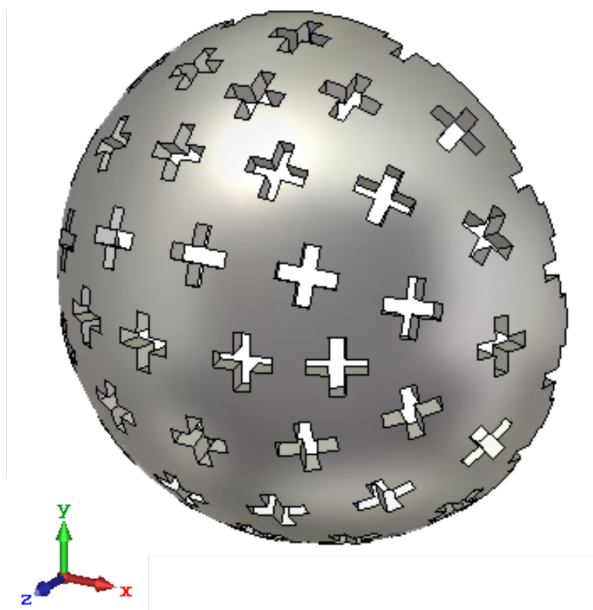
Figure 4.8: Ideal cross-dipole FSSs responses used as reference while designing spherical FSSs. Due to cross-dipole nature both TE and TM excitation responses overlap. Thus, only one is shown while leaving which one unlabeled.

Two figures of merit used in simulations to check the suitability of designs are monostatic RCS and transmission coefficient as defined in section 4.1.1. The first one gives insight of whether the structure is working as intended, meaning a dip at operating frequency should appear. The second one informs of the amount of EM wave able to cross the structure, which couples to the lens in a finished indoor tag.

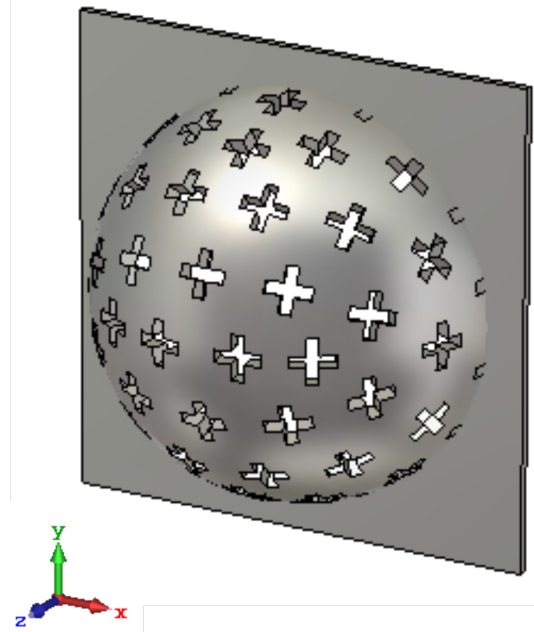
FSS with bucky ball pattern

The two simulations used to calculate structure response of the FSS are present in figure 4.9a and b. The former is used to obtain monostatic RCS, whereas the latter is used to calculate transmission coefficient. In figure 4.9b the creeping wave influence is eliminated, which gives clearer results.

Simulated monostatic RCS and transmission coefficient in terms of frequency are displayed in figure 4.10a and b, respectively. The first one is compared to original metallic semi sphere without elements engraved on it. There is a RCS minimum regarding semi sphere in the range of 75 GHz - 85 GHz (gray). In that area, FSS is operating as intended, by returning less power. However, its value is very similar regarding the reference half ball, since the largest difference is 5 dB. An explanation can be found in the transmission coefficient. From it, the FSS is operating not as stopband structure, but as a high-pass filter starting from 75 GHz. There are two possible reasons for this behavior. First, as aforementioned, width of slots is too large and thus they do not inhibit signal transmission at higher frequencies. Second, each cross-dipole presents a different resonant frequency, due to the angle of excitation of incoming wave. Thus, their resonating frequency is shifted towards lower values, which increases operating bandwidth in lower frequencies, and



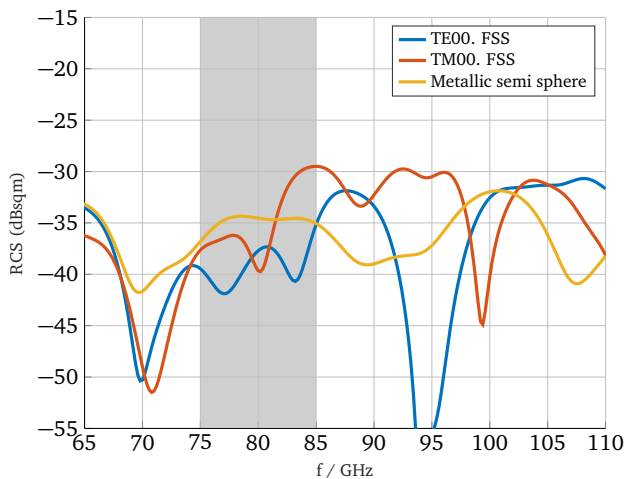
(a) Monostatic RCS simulation. Planar wave travels from +z to -z and its distance to structure is set to 2.5mm. Boundaries are set to open with background distance of 1mm.



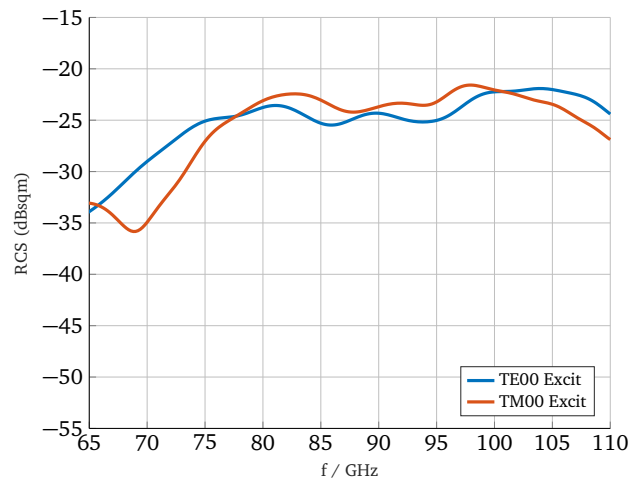
(b) Transmission simulation. Planar wave travels from +z to -z and its distance to structure is set to 2.5mm. Boundaries are set to open with background distance of 0mm. The metal plane divides simulation environment in half, effectively decoupling transmission response from creeping wave influence.

Figure 4.9: Simulation set ups for Bucky ball pattern FSS

their second-order passband resonances populate higher spectrum, contributing to the crossing of EM wave through the structure.



(a) Simulated monostatic RCS.



(b) Simulated transmission response

Figure 4.10: Simulated monostatic RCS and transmission for Bucky ball pattern FSS

FSS with custom pattern

The two simulations used to calculate structure response of the FSS are present in figure 4.11 a and b. The former is used to obtain monostatic RCS, whereas the latter is used to calculate transmission coefficient. Although both can be obtained from the first simulation, in b the creeping wave influence is eliminated, which gives clearer results.

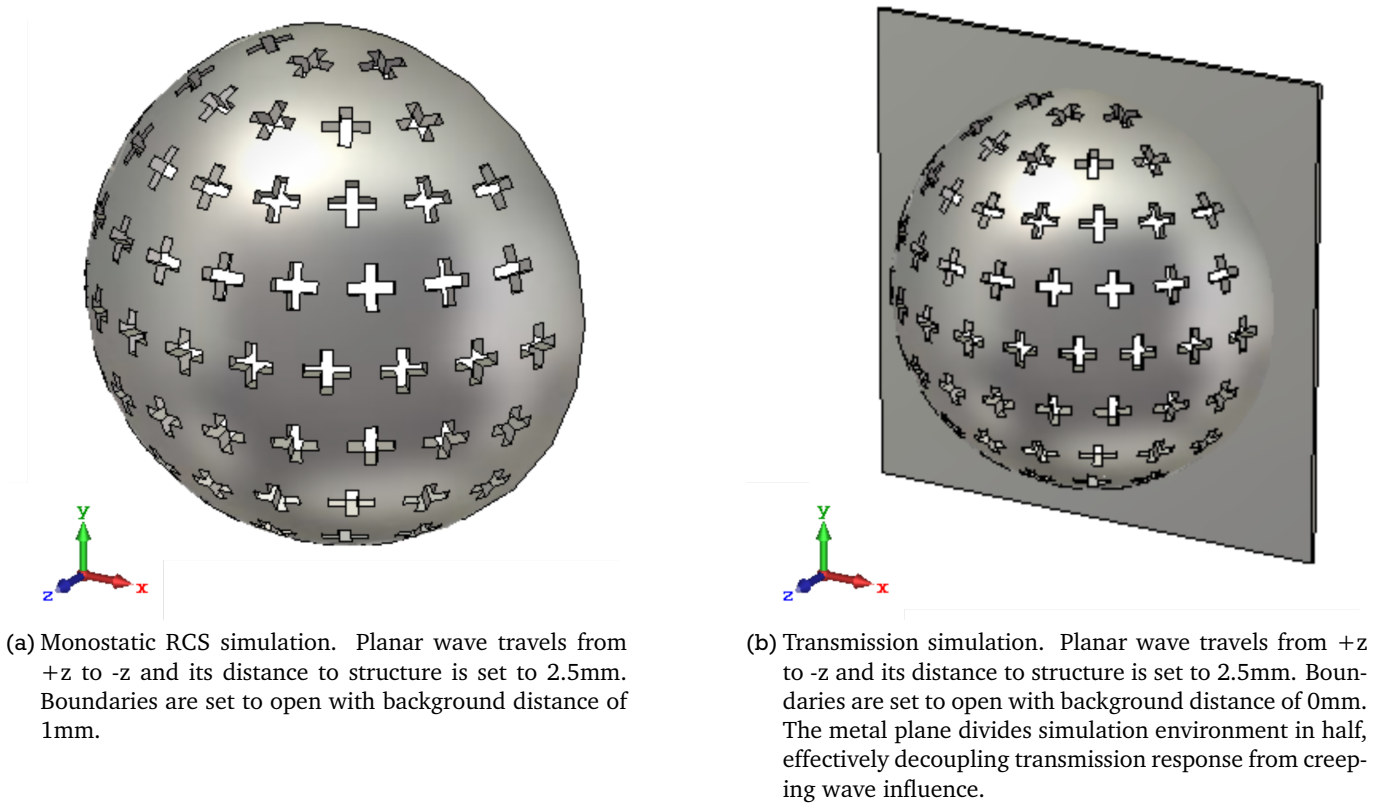


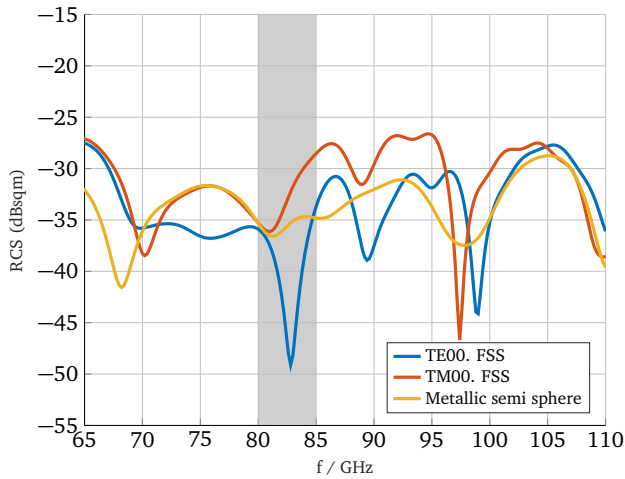
Figure 4.11: Simulation set ups for Custom pattern FSS

Simulated monostatic RCS and transmission coefficient in terms of frequency are displayed in figure 4.12a and b, respectively. The first one is compared to the original metallic semi sphere without elements engraved on it. There is a RCS minimum in the range of 80 GHz - 85 GHz, colored in gray. In that area, FSS is operating as intended, by not returning power. However, there is no clear resonance frequency. The explanation is the same as for the bucky pattern. Mainly, the large width of the elements and high-order passband resonances.

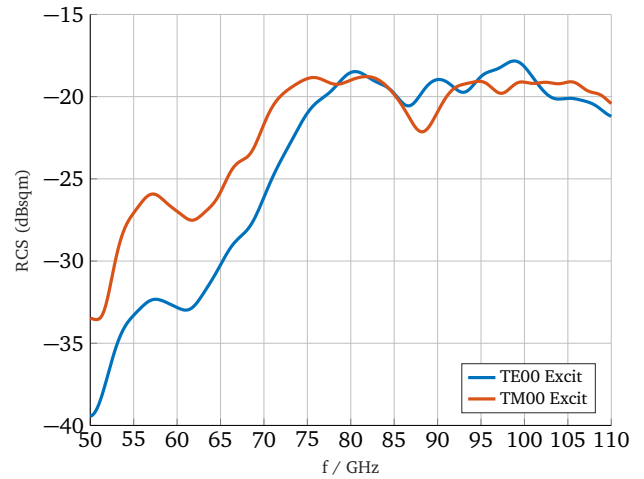
4.3 Fabricated structures and measured results

The two spherical FSSs presented in section 4.2.1 are printed along with their analogous metallic semi spheres, to close the structure around their corresponding lens. However, due to fabrication tolerances the structures are too small that lens do not fit inside them, which means that the tag cannot be closed. Therefore, in this section only characterization results for the fabricated structures, namely transmission and reflection coefficients, are presented.

The set up used to characterize the transmission coefficient of FSSs is similar to its analogous simulation environment presented in figures 4.9 and 4.11: a hole is done in a metal plane and then the FSS is attached



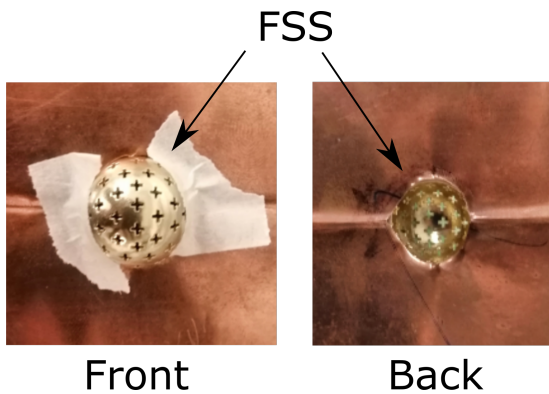
(a) Simulated monostatic RCS.



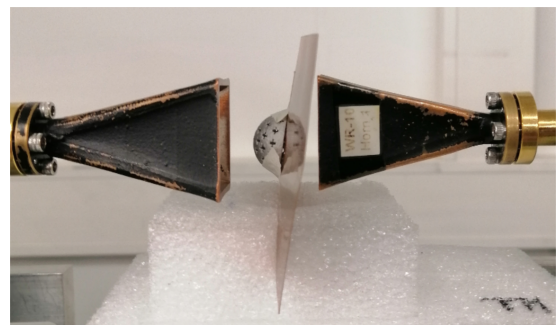
(b) Simulated transmission response

Figure 4.12: Simulated monostatic RCS and transmission for Custom pattern FSS

to that hole using tape. Afterwards, the whole structure is placed between two horn antennas. The horn antennas are located very close to each other, to achieve decoupling between both of them by means of the metal plane. Furthermore, time gating between 0 ns and 0.75 ns is used to clean the measured results. Figure 4.13 displays the aforementioned measurement set up.



(a) Structure attached to metal plane. Detachable adhesive tape is used to paste them.



(b) Measurement set up. As the antennas are very close to each other, the metal plane inhibits wave propagation between both.

Figure 4.13: Set up to measure transmission response of spherical FSSs

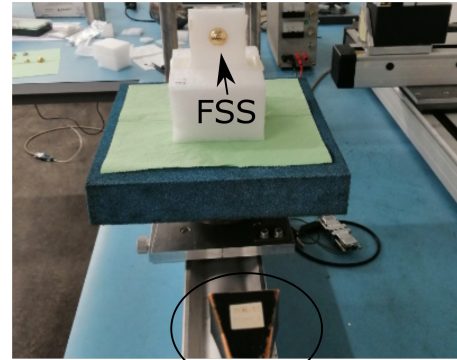
The set up to measure reflection response is the same as the one presented in section 3.3. The FSS is placed at 40 cm regarding the horn antenna and its reflection coefficient is cleaned using time gating between 2 ns and 4.7 ns. As the structures are spherical and need to be measured in frontal incidence, they are inserted in a dielectric slab that acts as support. Figure 4.14 shows this measurement set up.

4.3.1 Bucky ball pattern FSS

As aforementioned, bucky ball pattern FSS is designed to fit a lens with 15mm diameter. The structure is printed in two different materials, aluminum and brass, to check their suitability in mm-Wave applications and 3D printing accuracy while working with them. The fabricated FSSs, along with their corresponding half sphere, are displayed in figure 4.15 a and b.



(a) FSS inserted in dielectric slab. The slab influence is eliminated from results by including it in reference measurement that is then subtracted.

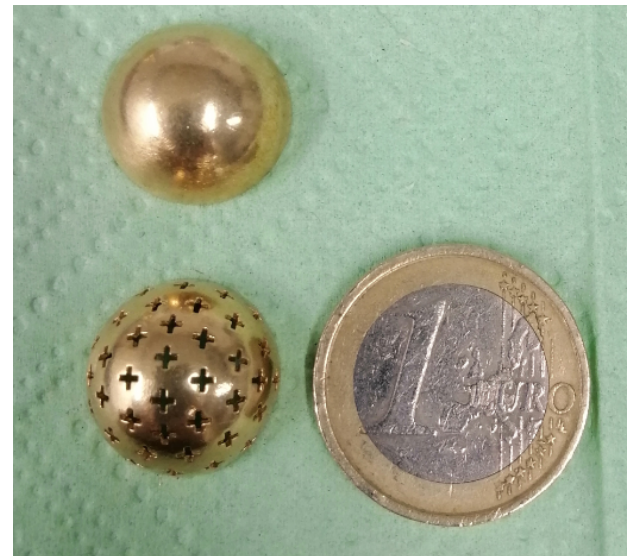


(b) Measurement set up. Horn antenna

Figure 4.14: Set up to measure reflection response of spherical FSSs



(a) Structures printed using aluminium as material.



(b) Structures printed using brass as material.

Figure 4.15: Printed spherical FSSs based on bucky ball pattern

The aluminum-based FSS presents inaccuracies in its fabrication that are observable without using amplifying equipment. Mainly, cross dipole slots on its surface are not straight, but have smoothed edges, particularly in the cross dipole's arms junction and corners. On the opposite, FSS made from brass does not show observable flaws. Thus, the second material is a better option when working at minimum feature size of metallic 3D printing technologies.

Measured transmission response for the structures fabricated with both materials is displayed in figure 4.16a and b. Furthermore, the raw response of the metal plane with hole is also shown. For both TE and TM polarized excitation, the addition of FSSs causes a different response than without them. First, the structures are not perfectly bandpass for one frequency, as their measured transmission coefficient has less amplitude than the metal plane without them (blue line). However, there is a clear transmission bandwidth for both FSS, although depending on the structure its maximum is located in different frequencies. For the aluminum-based FSS, the peak of transmission coefficient is at 95 GHz, whereas the brass-based one presents two maximum regarding the polarization of incoming wave, 82 GHz for TE excitation and 92 GHz for TM excitation. This difference owes to the metal plane, that presents a minimum in transmission for TM

polarization at 85 GHz, causing a dip in FSS response. Furthermore, the metal plane is also responsible for amplitude differences between transmission coefficient on both polarizations. TM-polarized waves present higher amplitude on average, owing to the hole made on the plane. Theoretically, a perfect circular hole presents same transmission for both polarizations, but it is cut with scissors directly on the metal plane, which introduces flaws.

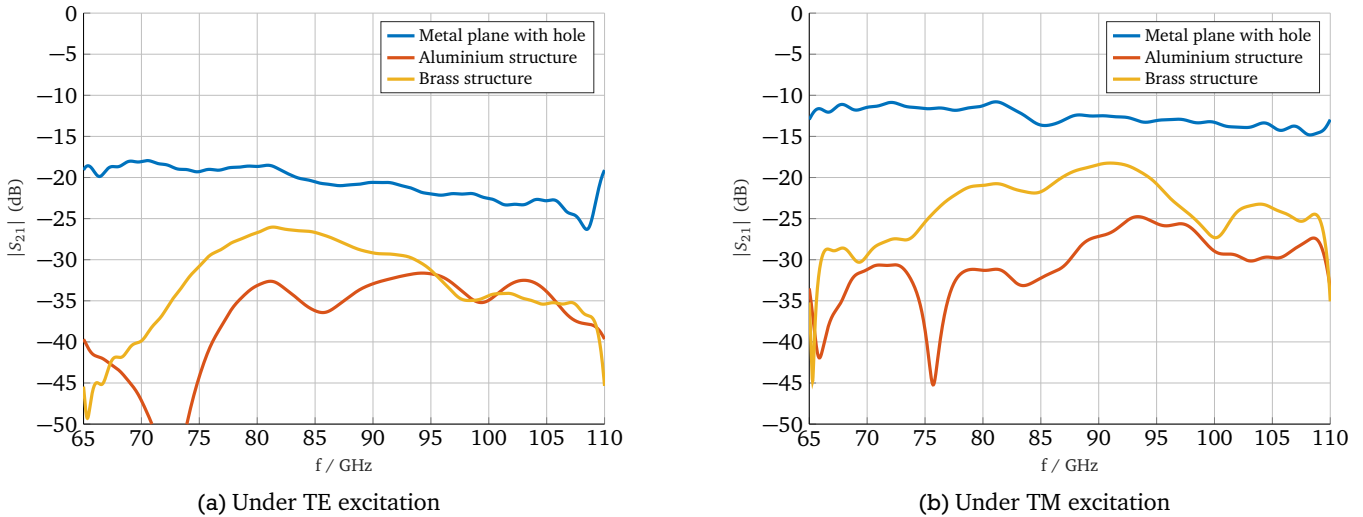


Figure 4.16: Measured transmission response for Bucky pattern FSSs

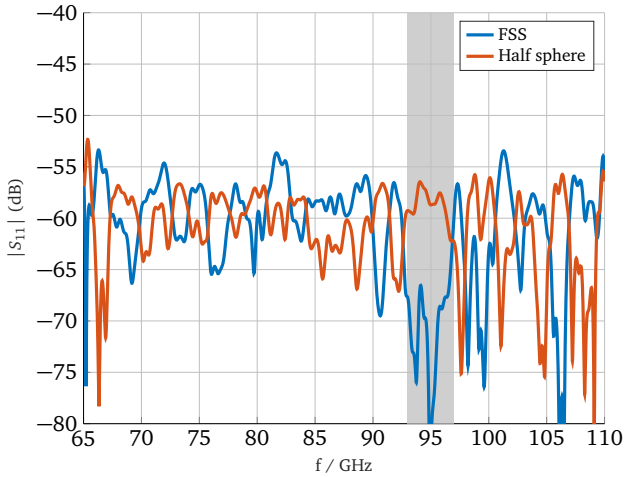
The reflection response of aluminium FSS and brass FSS is displayed in figure 4.17 and 4.18, respectively. The magnitude represented is the reflection coefficient instead of monostatic RCS, to showcase the very low amplitude that it presents. In most of the bandwidth, its measured amplitude is very close to the noise floor realizable by the used PNA, which is around -70 dB. Therefore, the results might be corrupted by environmental noise. In order to prevent this, FSSs' responses (blue line) is compared to its full metallic semi sphere (orange line) counterpart. In the aluminum structure, reflection coefficient presents a minimum for TE polarized waves on 95 GHz, colored with gray on figure 4.17a, which corresponds to the maximum on its transmission coefficient. However, it does not show conclusive response on TM excitation, where no differences are appreciable. Similar behavior is observed in brass-based FSS, whose reflection response under TE excitation presents a minimum at 85 GHz, whereas there are no observable differences under TM excitation.

4.3.2 Custom pattern FSS

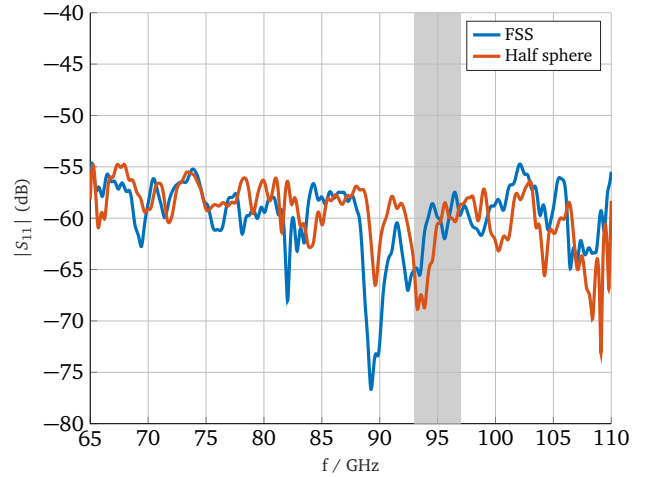
As aforementioned, the custom pattern FSS is designed to fit a lens of 20mm diameter but does not fit into the corresponding lens. As opposed to the previous FSS, this structure is printed only in brass. The fabricated FSS, along with their corresponding half sphere, is shown in figure 4.19. There are no observable flaws within the structure, which further confirms the suitability of brass in metal printed structures.

The measured transmission response for the FSS is displayed in figure 4.20a and b. Furthermore, the raw response of the metal plane with hole is also shown. For both TE and TM polarized excitation, the structure presents passband behavior between 75 GHz and 95 GHz, which is particularly observable in the results measured under TE excitation, since its amplitude is stable at -24 dB in whole bandwidth. Maximum transmission is reached at 85 GHz for both polarizations. As aforementioned, differences of amplitude are attributed to the flawed hole cut onto metal plane.

The measured reflection response for the FSS is displayed in figure 4.21a and b. Whereas the previous structures showed minimum under TE excitation, this FSS presents that behavior when excited by TM-polarized waves at 85 GHz. When TE excitation is considered, the reflected wave is below reference between

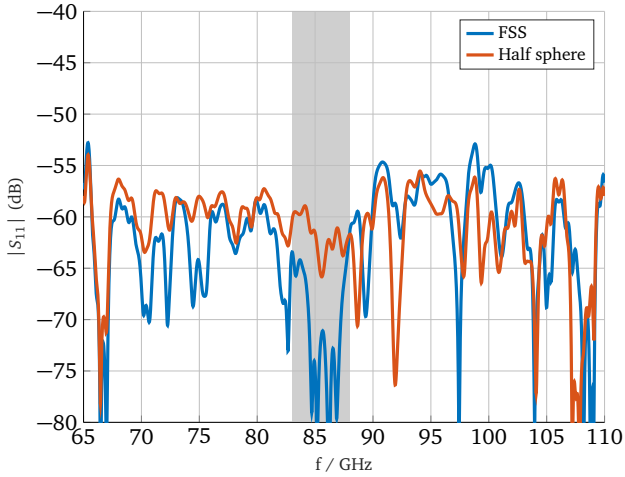


(a) Under TE-polarized wave.

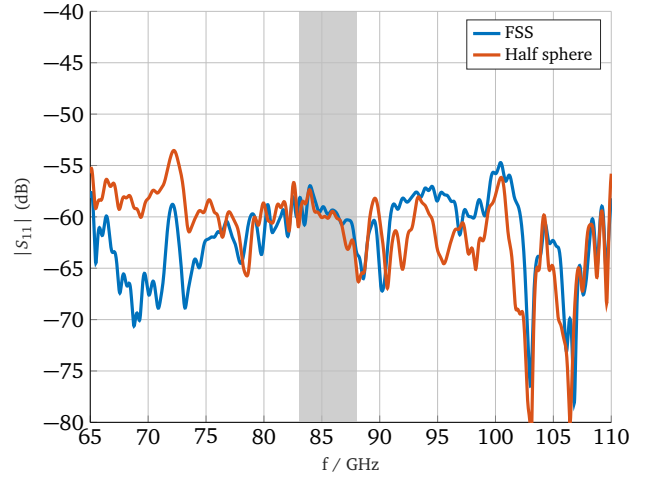


(b) Under TM-polarized wave.

Figure 4.17: Measured reflection response for aluminium-based bucky pattern FSSs



(a) Under TE-polarized wave.



(b) Under TM-polarized wave.

Figure 4.18: Measured reflection response for brass-based bucky pattern FSSs

87 GHz to 93 GHz. However, its behavior is the same as metallic semi sphere, but attenuated. Thus, it is not a guarantee that FSS is working properly in that range, as these differences might be due a small displacement between locations of FSS and metallic semi sphere when measured.

4.3.3 Discussion

During this section, two spherical FSS have been presented and measured to study their potential in indoor applications. They are summarized in table 4.2

	diameter (mm)	Pattern	Bandpass?	$\min(RCS_{\text{mono}})$
Aluminium	15	Bucky ball	✓	When TE ₀₀ wave, at 95 GHz
Brass	15	Bucky ball	✓	When TE ₀₀ wave, at 85 GHz
	20	Custom	✓	When TM ₀₀ wave, at 85 GHz

Table 4.2: Summary of results of spherical FSSs

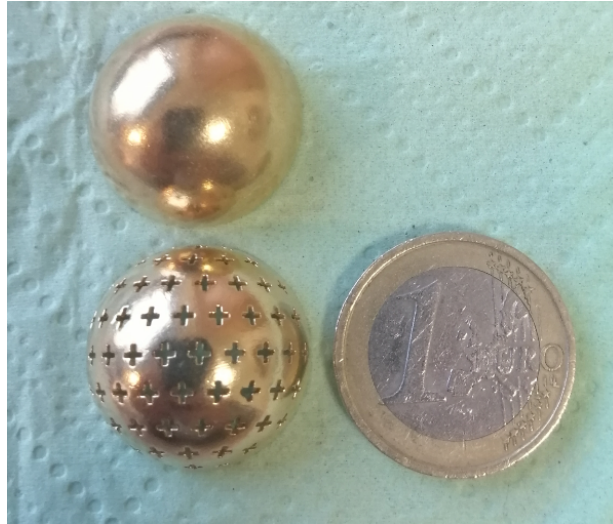


Figure 4.19: Printed spherical FSS based on custom pattern

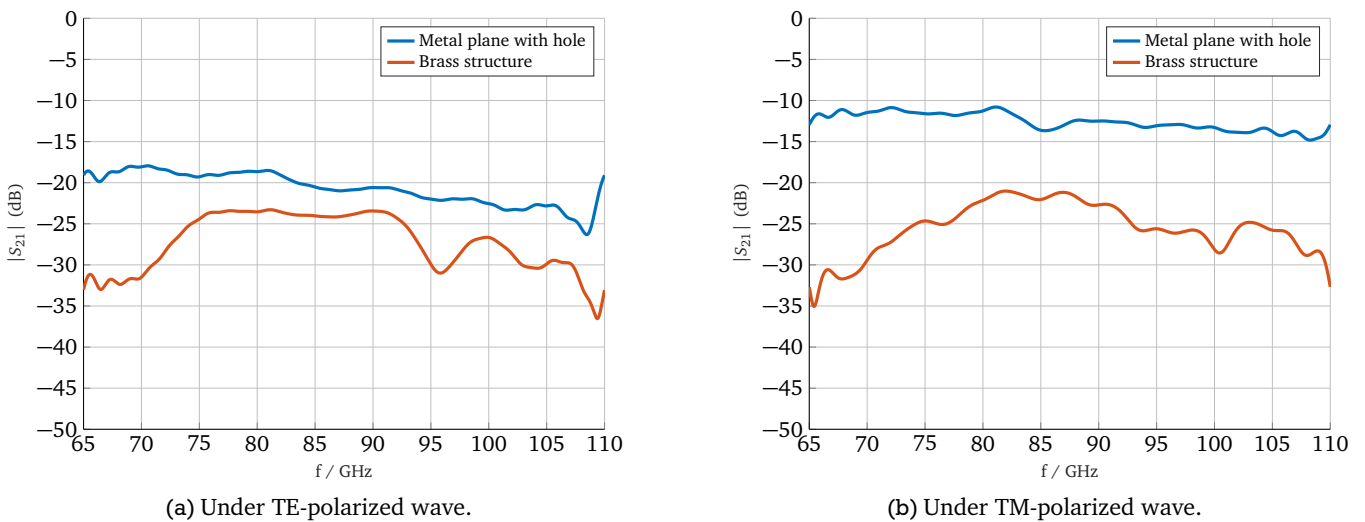


Figure 4.20: Measured transmission response for custom pattern FSS

One relevant result from the comparison between simulated and measured results is the difficulty to obtain similar monostatic RCS. The three fabricated structures present very different results than their simulated equivalences. However, transmission responses are quite similar in behavior, mainly wide bandpass-type bandwidth for both simulations and measurements. Therefore, one possibility to design such structures in the future is to rely on transmission simulations as presented in figures 4.9 and 4.11. However, this option does not account for the lens. As aforementioned in section 4.2, the FSS is meant to be integrated with lens whose ϵ_r is higher than air (around 4). The combination of FSS and lens shifts the frequency response of structure towards lower frequencies. In order to cope with the shift, FSS' element size needs to be rescaled to smaller values. Therefore, proper simulations of whole structure are also an option that should be considered. One disadvantage of using planar waves in such simulations using CST is that time gating is not possible, which could be useful to simulate the power coupling into retro reflector. To achieve this, waveguide ports combined with open boundaries need to be used. Thus, the excitation is not a planar wave, but it could be used to predict the structure response.

Regarding the use of 3D printing techniques, the resulting structures are satisfactory when using brass as base material. As previously shown, no appreciable flaws are observed. However, there is the limitation of minimum feature size. As aforementioned, the use of lens whose ϵ_r is higher than air (around 4) means

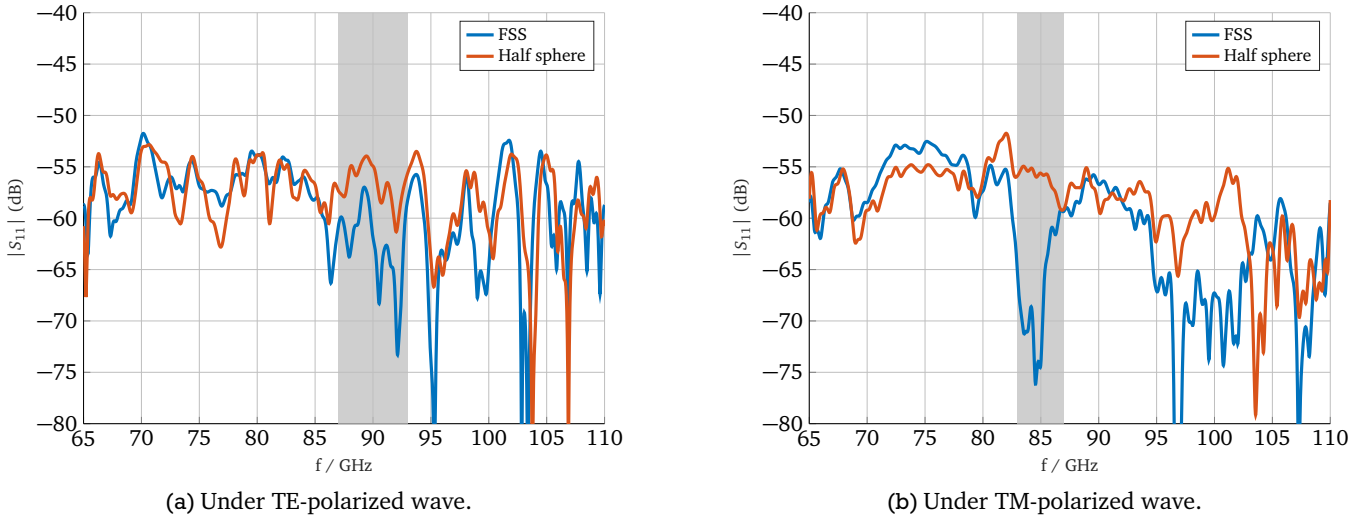


Figure 4.21: Measured reflection response for custom pattern FSS

that the structures have to be re-scaled smaller to maintain resonance frequency, which conflicts with current minimum achievable precision of 3D printing technologies, $500 \mu\text{m}$ [41] [42] [43]. Therefore, new fabrication options need to be considered, or the target operating frequency must be decreased.

The fabricated structures are promising when considering transmission coefficient. However, they present bandwidths that span between 10 GHz and 20 GHz, which means poor selectivity and very low bit resolution in practical applications. For instance, when a bandwidth of 10 GHz is considered, only four of such tags could be used in W-band (65 GHz to 110 GHz), which results in two bit resolution. These bandwidths are direct consequence of the shift in resonance frequency that cross dipoles present when being excited with planar wave with certain angle of arrival. Although only frontal excitation is used, the elements distributed along semi sphere surface are rotated regarding the structure axis, which causes the same effect as an incoming wave with oblique incidence in planar FSSs. Further designs to improve the selectivity of spherical structures should use elements whose resonance is stable independently of angle of incoming excitation wave. For instance, split ring resonators or their fractal versions can be milled or printed on curved metallic surfaces, while achieving resonance stability following the theory explained in chapter 3.

Finally, monostatic RCS of fabricated structures is not calculated, to showcase the low amount of power that these structures backscattered to the interrogating antenna. As RCS scales with geometrical size, structures are too small to obtain reliable results at 40 cm distance between them and interrogating antenna.

In light of the above, spherical FSSs show potential as a tool to achieve frequency selective behavior in lens-based retroreflectors. However, they present several limitations that need to be overcome. First, simulations are not yet a reliable possibility to predict structure behavior. Second, the designed spherical FSSs using cross dipoles present operating bandwidths of several GHz, which limits their application as indoor tag landmarks. Third, the fabricated structures present low reflection coefficient at selected measurement distance of 40 cm, which difficulties the obtaining of precise response. This can be improved by designing bigger spherical FSSs, which increases RCS, or further measurements on shorter range.

5 Conclusion and Outlook

In this work, two different approaches towards orientation-insensitive tag landmarks are presented. Both aim to achieve solutions for current limitations of passive indoor localization systems, which are frequency behavior and amplitude instability regarding angle of incidence of incoming wave and specular reflection indetermination. First, planar structures with stable resonance are presented. Then, the suitability of spherical FSSs in indoor localization systems is discussed.

The planar structures presented in chapter 3 are designed to achieve stable resonance. The shift in FSS' resonance frequency owing to oblique incidence is discussed and several solutions are proposed. The chosen one is to miniaturize two classical FSS unit cells (square and circular ring) and their complementary structures by enclosing them with a grid. By doing so, gridded FSS are 42% smaller for classical FSS and 31% for complementary. The structure with best performance when combined with CR is the complementary gridded circular ring under TM₀₀ excitation. Its frontal resonance frequency is 79.30 GHz, and it lies in a relative bandwidth of 2.22% around that frequency, when changing the incoming wave angle up to $\pm 40^\circ$. In absolute values, this means a bandwidth of 1.8 GHz, allowing for the use of 40 of these tags in W-band. Nevertheless, the structure with worst response, gridded square ring, featured a relative bandwidth of 6.87% around a central frequency of 77.86 GHz, meaning an absolute value of 5.2 GHz. In this case, only 8 tags can be used on W-band. In general, circular ring designed show a more stable frequency response than their square counterparts. Nevertheless, all measured tag landmarks show good monostatic RCS, which varies between -8 dB and -20 dB depending of angle of excitation. Therefore, the system is not constrained by range in indoor applications.

However, the aforementioned structures present several limitations. First, their frequency selectivity has to be improved to achieve practical applications. For instance, the designed passband structures do not present a clear resonance frequency, and the stopband ones shows wide and shallow bandwidths in frontal excitation. Second, due to specular reflection and CR shortcomings, they work in a limited angular domain, between 10° and 40° regarding frontal incidence.

As an outlook, improvement on RCS and frequency selective behavior has to be carried out. First, the structures should be designed so their resonances are contrary to their natural behavior. This means stopband resonance in normal structures and passband behavior in complementary ones. Second, as it has been show that miniaturization works when achieving resonance stability, new designs such as fractal unit cells can be explored to improve these shortcomings.

In this work, a first approach to design spherical tag landmarks is carried out. First, the theory behind such systems is described. Second, a program able to automatically generate such structures in CST is developed. Third, two designed FSSs are 3D-printed in metallic materials, aluminium and brass, and their performance is measured. From the results, brass is a better option when working with minimum feature size of metallic printing technologies.

The first measurements of the fabricated devices show promising results. The brass based-structures present transmission responses centered at 85 GHz as it is intended, although their bandwidth spans several GHz. Moreover, their RCS is measured at a distance of 40 cm, and presents minimum at that frequency, as intended. However, this only happens for certain excitations. It is suspected that the reason is their extremely low RCS, causing the results to be mixed by clutter. However, further designs and measurements are needed to confirm this theory. In addition, other limitation is that current simulations do not predict properly the response of such structures, which difficult their design. Furthermore, minimum feature size achievable with

metallic 3D-printing technology is too large to have complete freedom on design of structures that operate at 85 GHz.

Future work should focus on different approaches. First, measure the structures' responses in shorter distances. Second, search for technologies that allow for smaller structures to be fabricated, such as electroplating combined with highly precise dielectric 3D printing techniques. Another option is to design such FSSs at lower frequencies, which overcomes the minimum feature size limitation. Third, since the spherical FSS is meant to be integrated with a lens-based retroreflector, future designs should consider the frequency shift caused by lens' ϵ_r on them in the design process. This further aggravates the problem of minimum feature size at 85 GHz, as the elements of FSSs need to be rescaled smaller to compensate for the aforementioned frequency shift.

A Custom MATLAB - CST functions

The functions presented here are meant to complement toolbox's [40] capabilities and use its same naming scheme.

Function to subtract objects in CST.

```
1 function subtractObject(obj,object1,object2)
2 %Subtract object2 from object1
3 VBA = sprintf('Solid.Subtract "%s", "%s"',object1,object2);
4 obj.update(sprintf('Boolean Subtract Shapes:%s,%s',object1,object2),VBA);
5 end
```

Function to add objects in CST.

```
1 function sumObject(obj,object1,object2)
2 %Add object2 to object1
3 VBA = sprintf('Solid.Add "%s", "%s"',object1,object2);
4 obj.update(sprintf('Boolean Add Shapes:%s,%s',object1,object2),VBA);
5 end
```

Function to define planar wave excitation in CST

```
1 function addLinearPlanewave(obj,X,Y,Z,Ex,Ey,Ez,refFreq)
2 % Adds linear planewave
3 VBA = sprintf(['With PlaneWave\n',...
4 '.Reset\n',...
5 '.Normal "%d","%d","%d"\n',...
6 '.EVector "%d", "%d", "%d"\n',...
7 '.Polarization "Linear" \n',...
8 '.ReferenceFrequency "%f"\n',...
9 '.PhaseDifference "-90.0"\n',...
10 '.CircularDirection "Left"\n' ...
11 '.AxialRatio "0.0" \n' ...
12 '.SetUserDecouplingPlane "False"\n',...
13 '.Store\n', ...
14 'End With'],...
15 X,Y,Z,Ex,Ey,Ez,refFreq);
16 obj.update(['define plane wave properties'],VBA);
17 end
```

Modification of "addBrick" function, to be able to use string parameters as inputs. Comment the following lines:

```
1 % Deleted to accept CST parameters with mathematical operations
2 %           X = obj.checkParam(X);
3 %           Y = obj.checkParam(Y);
4 %           Z = obj.checkParam(Z);
```

Modification of "rotateObject" function, to accept grouping objects as an input, and correct problems that arise with toolbox 2019 version.

```
1 function rotateObject(obj,varargin) % Modified from toolbox to solve old ...
   version compatibility problems with CST (2019)
2 % CST.rotateObject(objectName,rotationAngles,rotationCenter)
3 % Rotates an object defined by objectname of the format
4 % (componentName:objectName) by the rotation angle
5 % in rotationAngles = [xrot, yrot, zrot] and the center of
6 % rotation defined be rotationCenter = [xc, yc,zc];
7 if ischar(varargin{2})
8 nameStr = [varargin{1},':',varargin{2}];
9 varargin(2) = [];
10 else
11 nameStr = varargin{1};
12 end
13 [rotationAngles,rotationCenter] = deal(varargin{2:3});
14 varargin(1:3) = [];
15
16 %Modified to include grouping option
17 p = inputParser;
18 p.addParameter('copy',false);
19 p.addParameter('group',false);
20 p.addParameter('repetitions',1);
21 p.parse(varargin{:});
22
23 copy = p.Results.copy;
24 group = p.Results.group;
25 repetitions = p.Results.repetitions;
26
27 if copy
28 copyStr = 'True';
29 else
30 copyStr = 'False';
31 end
32 if group
33 groupStr = 'True';
34 else
35 groupStr = 'False';
36 end
37
38 rotationAngles = obj.checkParam(rotationAngles);
39 rotationCenter = obj.checkParam(rotationCenter);
40
41 VBA = sprintf(['With Transform\n',...
42 '.Reset\n',...
43 '.Name "%s"\n',...
44 '.Origin "Free"\n',...
45 '.Center "%s", "%s", "%s"\n',...
46 '.Angle "%s", "%s", "%s"\n',...
47 '.MultipleObjects "%s"\n',...
48 '.GroupObjects "%s"\n',...
49 '.Repetitions "%d"\n',...
50 '.MultipleSelection "False"\n',...
51 '.Transform "Shape", "Rotate"\n',...
52 'End With'],...
53 nameStr,rotationCenter(1),rotationCenter(2),rotationCenter(3),...
54 rotationAngles(1),rotationAngles(2),rotationAngles(3),...
55 copyStr,groupStr,repetitions);
56
57 obj.update(['transform: rotate ',nameStr],VBA);
58 end
```

B Creation of cross-dipole in CST from MATLAB

Code to create dipole element.

```
1 % 1. Create slab centered at (0,0,0)
2 Xblock = {'-element_length/2' 'element_length/2'};
3 Yblock = {'-element_width/2' 'element_width/2'};
4 Zblock = {'-element_thickness' 'element_thickness'};
5 material = 'Vacuum';
6 component = 'Component2';
7 name = ['CrossDip_', num2str(n)];
8 full_name = char(strcat(component, ":", name));
9 CST.addBrickModified(Xblock, Yblock, Zblock, name, component, material); %Note - you ...
    must always use unique names
10 % 2. Create second arm and add together
11 CST.rotateObject(component, name, {0 0 90}, [0 0 0], 'copy', true, 'group', true)
12 % 3. Move to (0,0,radius)
13 CST.translateObject(full_name, 0, 0, sphere_radius, 0);
14 % 4. Rotate. Rotations already calculated on rotated(n)
15 %- Rotation must be done axis per axis. ORDER OF ROTATIONS: YZ . Right hand ...
    rotation system
16 CST.rotateObject(component, name, {0 rotated(n).alpha 0}, [0 0 ...
    0], 'copy', false, 'group', false); % OY rotation
17 CST.rotateObject(component, name, {0 0 rotated(n).beta}, [0 0 ...
    0], 'copy', false, 'group', false); % OZ rotation
18 % 5. Boolean subtract
19 CST.subtractObject('Component1:outer_shell', [component, ':', name]);
```

Code to create tripole element.

```
1 % 1. Create slab centered at (0,0,0)
2 Xblock = {'-element_width/2' 'element_width/2'};
3 Yblock = {'0' 'element_length/2'}; % Will this work?
4 Zblock = {'-element_thickness' 'element_thickness'};
5 material = 'Vacuum';
6 component = 'Component2';
7 name = ['Trip_', num2str(n)];
8 full_name = char(strcat(component, ":", name));
9 CST.addBrickModified(Xblock, Yblock, Zblock, name, component, material); %Note - you ...
    must always use unique names
10 % 2. Create second and third arm and add together
11 CST.rotateObject(component, name, {0 0 120}, [0 0 0], 'copy', true, 'group', true);
12 CST.rotateObject(component, name, {0 0 120}, [0 0 0], 'copy', true, 'group', true);
13 % 3. Move to (0,0,radius)
14 CST.translateObject(full_name, 0, 0, sphere_radius, 0);
15 % 4. Rotate. Rotations already calculated on rotated(n)
16 %- Rotation must be done axis per axis. ORDER OF ROTATIONS: YZ . Right hand ...
    rotation system
17 CST.rotateObject(component, name, {0 rotated(n).alpha 0}, [0 0 ...
    0], 'copy', false, 'group', false); % OY rotation
18 CST.rotateObject(component, name, {0 0 rotated(n).beta}, [0 0 ...
    0], 'copy', false, 'group', false); % OZ rotation
19 % 5. Boolean subtract
20 CST.subtractObject('Component1:outer_shell', [component, ':', name]);
```




C Custom FSS pattern

```
1 function V = customFSSPositions(sphere_radius,a)
2 % Input : sphere_radius and a, which is unit cell separation.
3 % Output: Location of FSS elements in a vector V(Nelements,3), where 3 are ...
4 % the x, y ,z coordinates
5 % The top half of the sphere is calculated and then mirrored.
6 %- Calculate numer of UCs in height (Y plane, following CST convention)
7 length_halfCirc = pi*sphere_radius/2; % In reality, is half of the half ...
8 % circle, as this calculates layers in height.
9 if rem(length_halfCirc,a) % If no natural division
10 Nold = length_halfCirc/a;
11 N = floor(Nold);
12 py = length_halfCirc/N;
13 msg = sprintf('--> No natural number of UCs possible on sphere surface. ...
14 % Y-period adjusted. ');
15 %disp(msg);
16 msg = sprintf('--> Old period %.3f. New period %.3f', a,py);
17 %disp(msg);
18 readjust = abs((py-a)/a)*100;
19 msg = ['-> Adjusted to ' num2str(readjust) ' % of original size'];
20 %disp(msg);
21 else
22 N = length_halfCirc/a;
23 py = a;
24 end
25 msg = sprintf('Number of UC layers within half sphere: %.3f with period: ...
26 % %.3f',N,py);
27 disp(msg);
28
29 %- Calculate position of cutting XZ planes
30 cutPlanes = sphere_radius*sin((py/sphere_radius).*(0:N));
31 finalPlane = N;
32
33 %- Calculate position of superior half sphere.
34 % Sphere is assumed to be centered at (0,0,0).
35 V = [0 0 0]; % Initialize element location
36 for n = 1:finalPlane
37 D = cutPlanes(n); % "Height" of cut circle
38 rCut = sqrt(sphere_radius.^2-D.^2); % Radius of the cut circle
39 length_cutCirc = 2*pi*rCut;
40 %- Adjust XZ period so natural number of UCs fits on circle
41 if rem(length_cutCirc,a) % If no natural division
42 nUCs_old = length_cutCirc/a;
43 nUCs = floor(nUCs_old);
44 pxz = length_cutCirc/nUCs;
45 msg = sprintf('--> No natural number of UCs possible on sphere surface. ...
46 % XZ-period adjusted. ');
47 %disp(msg);
48 msg = sprintf('--> Old period %.3f. New period %.3f', a,pxz);
49 %disp(msg);
50 readjust = abs((pxz-a)/a)*100;
51 msg = ['-> Adjusted to ' num2str(readjust) ' % of original size'];
52 %disp(msg);
53 else
```

```

49     nUCs = length_cutCirc/a;
50     pxz = a;
51     end
52     %- Calculate angles where the center of UCs are located (element
53     % position)
54     if rem(nUCs,2) % Odd number
55         t = 0:(2*pi/nUCs):2*pi;
56     else % Even number
57         t = 0.5*(2*pi/nUCs):(2*pi/nUCs):2*pi;
58     end
59     %- Calculate element cartesian coordinates
60     for u = 1:length(t)
61         V(end+1,:) = [rCut.*cos(t(u)), ... % X coord
62         rCut.*sin(t(u)), ... % Y coord
63         D]; % Z coord
64     end
65     end
66     V(1,:) = []; % Delete initialization
67
68     %- Calculate the other half sphere positions
69     % Its just to duplicate everything but with y coords negative
70     Vaux = [V(:,1) V(:,2) -V(:,3)];
71     V = [V ; Vaux];
72     end

```

Bibliography

- [1] A. Alarifi, A. Al-Salman, M. Alsaleh, A. Alnafessah, S. Al-Hadhrami, M. Al-Ammar, and H. Al-Khalifa, "Ultra wideband indoor positioning technologies: Analysis and recent advances," *Sensors*, vol. 16, no. 5, p. 707, May 2016. [Online]. Available: <http://dx.doi.org/10.3390/s16050707>
- [2] G. Lachapelle, "Gnss indoor location technologies," *Journal of Global Positioning Systems*, vol. 3, pp. 2–11, 2004.
- [3] R. Mautz, "The challenges of indoor environments and specification on some alternative positioning systems," *2009 6th Workshop on Positioning, Navigation and Communication*, 2009.
- [4] J. Xiong, K. Sundaresan, and K. Jamieson, "Tonetrack: Leveraging frequency-agile radios for time-based indoor wireless localization," *Proceedings of the 21st Annual International Conference on Mobile Computing and Networking - MobiCom 15*, 2015.
- [5] A. Jiménez-Sáez, M. Schüßler, D. Pandel, N. Benson, and R. Jakoby, "3d printed 90 ghz frequency-coded chipless wireless rfid tag," in *2019 IEEE MTT-S International Microwave Workshop Series on Advanced Materials and Processes for RF and THz Applications (IMWS-AMP)*, July 2019, pp. 4–6.
- [6] A. Ramos, A. Lazaro, D. Girbau, and R. Villarino, "Time-domain measurement of time-coded uwb chipless rfid tags," *Progress In Electromagnetics Research*, vol. 116, pp. 313–331, 2011.
- [7] M. Schüßler, C. Mandel, M. Maasch, A. Giere, and R. Jakoby, "Phase modulation scheme for chipless rfid- and wireless sensor tags," in *2009 Asia Pacific Microwave Conference*, Dec 2009, pp. 229–232.
- [8] A. Jiménez-Sáez, M. Schüßler, M. Nickel, and R. Jakoby, "Hybrid time-frequency modulation scheme for chipless wireless identification and sensing," *IEEE Sensors Journal*, vol. 18, no. 19, pp. 7850–7859, Oct 2018.
- [9] M. El-Absi, A. Alhaj Abbas, A. Abuelhaija, F. Zheng, K. Solbach, and T. Kaiser, "High-accuracy indoor localization based on chipless rfid systems at thz band," *IEEE Access*, vol. 6, pp. 54 355–54 368, 2018.
- [10] R. S. Anwar, L. Mao, and H. Ning, "Frequency selective surfaces: A review," *Applied Sciences*, vol. 8, no. 9, 2018. [Online]. Available: <https://www.mdpi.com/2076-3417/8/9/1689>
- [11] A. Jiménez-Sáez, M. Schüßler, M. El-Absi, A. Alhaj Abbas, K. Solbach, T. Kaiser, and R. Jakoby, "Frequency selective surface coded retroreflectors for chipless indoor localization tag landmarks," *IEEE*, 2018.
- [12] M. Skolnik, *Radar handbook*. McGraw-Hill, 1970.
- [13] N. C. Currie and C. E. Brown, *Principles and applications of millimeter-wave radar*. Artech House, 1987.
- [14] Z. Tarique, W. Q. Malik, and D. J. Edwards, "Bandwidth requirements for accurate detection of direct path in multipath environment," *Electronics Letters*, vol. 42, no. 2, pp. 100–102, Jan 2006.
- [15] D. M. Pozar, *Microwave engineering, 4th edition*. John Wiley & Sons, 2011.
- [16] A. W. Doerry, "Reflectors for sar performance testing." Jan 2008.

-
- [17] R. Wang, Y. Qin, B. Deng, and H. Wang, "Radar cross section of the metal sphere from microwave to the optical frequency," *2014 39th International Conference on Infrared, Millimeter, and Terahertz waves (IRMMW-THz)*, 2014.
- [18] P. S. P. Wei, "Radar echoes from metal spheres large and small," *AMTA 2016 Proceedings*, 2016.
- [19] R. J. Williams, "Frequency selective terahertz retroreflectors," Ph.D. dissertation, Department of physics and applied physics, University of Massachusetts, 2014.
- [20] P. Schumacher, C. Schuster, A. Jiménez-Sáez, M. Schüßler, and R. Jakoby, "Passive chipless wireless pressure sensor for harsh and reflective environments," in *2018 11th German Microwave Conference (GeMiC)*, March 2018, pp. 227–230.
- [21] S. Celozzi, R. Araneo, and G. Lovat, *Electromagnetic shielding*. Wiley-Interscience, 2008.
- [22] M. Gustafsson, A. Karlsson, A. Rebelo, and B. Widenberg, "Design of frequency selective windows for improved indoor outdoor communication," *IEEE Transactions on Antennas and Propagation*, vol. 54, no. 6, p. 1897–1900, 2006.
- [23] W. Mohyuddin, D. Kim, H. Choi, and K. Kim, "Comparative study of square and circular loop frequency selective surfaces for millimeter-wave imaging diagnostics systems," *Sensors*, vol. 18, no. 9, p. 3079, 2018.
- [24] H. Zhou, S.-B. Qu, B.-Q. Lin, J.-Q. Zhang, C. Gu, H. Ma, Z. Xu, P. Bai, and W.-D. Peng, "Dual band frequency selective surface based on circular aperture-coupled patches," *Microwave and Optical Technology Letters*, vol. 53, no. 8, p. 1784–1786, 2011.
- [25] D. F. Pieper, "Application of embedded frequency selective surfaces for structural health monitoring," Ph.D. dissertation, 2016.
- [26] E. A. Parker, "The gentleman's guide to frequency selective surfaces." *University of Kent, Kent, UK*, 1991.
- [27] T. K. Wu, *Frequency selective surface and grid array*. Wiley, 1995.
- [28] V. Agrawal and W. Imbriale, "Design of a dichroic cassegrain subreflector," *IEEE Transactions on Antennas and Propagation*, vol. 27, no. 4, p. 466–473, 1979.
- [29] T. K. Wu, "Improved dual band fss performance with fractal elements," *Microwave and Optical Technology Letters*, vol. 54, no. 3, p. 833–835, 2012.
- [30] T.-K. Wu, "Angle of incidence-stable fss with dsrs elements," *2019 URSI International Symposium on Electromagnetic Theory (EMTS)*, 2019.
- [31] G. Yang, T. Zhang, W. Li, and Q. Wu, "A novel stable miniaturized frequency selective surface," *IEEE Antennas and Wireless Propagation Letters*, vol. 9, p. 1018–1021, 2010.
- [32] X. F. Luo and C. K. Lee, "Design of dual-band frequency selective surfaces with gridded-square elements," *Proceedings of the 2008 International Conference on Advanced Infocomm Technology - ICAIT 08*, 2008.
- [33] C. Lee and R. Langley, "Equivalent-circuit models for frequency-selective surfaces at oblique angles of incidence," *IEE Proceedings H Microwaves, Antennas and Propagation*, vol. 132, no. 6, p. 395, 1985.
- [34] G. I. Kiani, K. P. Esselle, K. L. Ford, A. R. Weily, and C. Panagamuwa, "Angle and polarization-independent bandstop frequency selective surface for indoor wireless systems," *Microwave and Optical Technology Letters*, vol. 50, no. 9, p. 2315–2317, 2008.
- [35] A. Ebrahimi, R. T. Ako, W. S. L. Lee, M. Bhaskaran, S. Sriram, and W. Withayachumnankul, "High-q terahertz absorber with stable angular response," *IEEE Transactions on Terahertz Science and Technology*, vol. 10, no. 2, p. 204–211, 2020.

-
- [36] S. N. Azemi, T. Baum, K. Ghorbani, and W. S. Rowe, "3d-tapered resonators for fsss with incident angle independence," *IET Microwaves, Antennas & Propagation*, Aug 2017.
- [37] S. Skokic and Z. Sipus, "Moment method analysis of a spherical fss in free space," *2005 18th International Conference on Applied Electromagnetics and Communications*, 2005.
- [38] Z. Sipus, M. Bosiljevac, and S. Skokic, "Analysis of curved frequency selective surfaces," 2008.
- [39] I.-P. Hong and I.-G. Lee, "Comparisons of rcs characteristic of spherical frequency selective surfaces with fss element arrangement," *Journal of IKEEE*, vol. 16, no. 4, p. 328–334, 2012.
- [40] Hgiddens, 2019. [Online]. Available: https://www.github.com/hgiddens/CST_App
- [41] "How to design parts for metal 3d printing," Visited: 10th April 2020. [Online]. Available: <https://www.3dhubs.com/knowledge-base/how-design-parts-metal-3d-printing/#limitations>
- [42] "What is the smallest feature that you can print?" Visited: 10th April 2020. [Online]. Available: <https://support.xometry.com/hc/en-us/articles/217723698-What-is-the-smallest-feature-that-you-can-print->
- [43] "3d metal printing: tips, trends and common misconceptions," Visited: 10th April 2020. [Online]. Available: <https://www.machinedesign.com/3d-printing-cad/article/21835806/3d-metal-printing-tips-trends-and-common-misconceptions>



List of Figures

1.1	Sketch of generic indoor self-localizing system.	5
1.2	Self-localizing monostatic radar system in frequency domain, from [11]	7
2.1	Differences between mirror and retroreflectors and most common retroreflectors.	12
2.2	Sketch of time gating technique	13
2.3	Bandstop and bandpass FSS using cross-dipoles.	14
3.1	Illustration of TE and TM incidence, from [25]	15
3.2	Designed gridded square ring FSS and its response.	18
3.3	Comparison between classical square ring and gridded design regarding resonance stability.	18
3.4	Designed gridded circular ring FSS and its response.	19
3.5	Comparison between classical circular ring and gridded design regarding resonance stability.	20
3.6	Designed complementary gridded square ring FSS and its response.	20
3.7	Comparison between complementary classical square ring and gridded design regarding resonance stability.	21
3.8	Designed complementary gridded circular ring FSS and its response.	22
3.9	Comparison between complementary classical circular ring and gridded design regarding resonance stability.	22
3.10	Measurement set up for characterization of FSSs	23
3.11	Fabricated passband FSSs	23
3.12	Measured transmission coefficient for frontal incidence in passband structures.	23
3.13	Measured transmission coefficient for angle of incidence between -45° to 45° , with 5° steps, in passband structures.	24
3.14	Fabricated stopband FSSs	25
3.15	Measured transmission coefficient for frontal incidence in stopband structures.	25
3.16	Measured resonant frequency for angle of incidence between -45° to 45° , with 5° steps, in stopband structures.	25
3.17	Measured transmission coefficient for angle of incidence between -45° to 45° , with 5° steps, in stopband structures.	26
3.18	Corner reflector and FSS	27
3.19	Measured reflection coefficient for passband square ring FSS with corner reflector	28
3.20	Measured reflection coefficient for passband circular ring FSS with corner reflector	28
3.21	Measured RCS for passband tags at 75 GHz	29
3.22	Measured reflection coefficient for stopband square ring design with corner reflector	29
3.23	Measured reflection coefficient for stopband circular ring design with corner reflector	30
3.24	Measured resonance frequency regarding angle of excitation for stopband designs	30
3.25	Measured RCS for stopband tags at 100 GHz	31
3.26	Comparison between complementary gridded square FSS and classical cross-dipole FSS	32
4.1	Passband spherical FSS [39]	34
4.2	Example of two spherical FSS	35
4.3	Sketch of connection between MATLAB and CST	35
4.4	Flowchart of the process to generate spherical FSS	36
4.5	MATLAB output of spherical FSSs with 15mm diameter using different element patterns.	37
4.6	CST output of spherical FSSs with 15mm diameter using different element patterns.	37

4.7	Working principle of spherical tag landmark	39
4.8	Ideal cross-dipole FSSs responses used as reference while designing spherical FSSs	40
4.9	Simulation set ups for Bucky ball pattern FSS	41
4.10	Simulated monostatic RCS and transmission for Bucky ball pattern FSS	41
4.11	Simulation set ups for Custom pattern FSS	42
4.12	Simulated monostatic RCS and transmission for Custom pattern FSS	43
4.13	Set up to measure transmission response of spherical FSSs	43
4.14	Set up to measure reflection response of spherical FSSs	44
4.15	Printed spherical FSSs based on bucky ball pattern	44
4.16	Measured transmission response for Bucky pattern FSSs	45
4.17	Measured reflection response for aluminium-based bucky pattern FSSs	46
4.18	Measured reflection response for brass-based bucky pattern FSSs	46
4.19	Printed spherical FSS based on custom pattern	47
4.20	Measured transmission response for custom pattern FSS	47
4.21	Measured reflection response for custom pattern FSS	48

List of Tables

1.1	Popular technologies and their spatial resolution [4]	6
3.1	Dimensions of gridded square ring unit cell.	17
3.2	Dimensions of gridded circular ring unit cell.	19
3.3	Comparison between simulated and measured resonance stability.	26
3.4	Relative frequency shift for operating region of stopband FSS tag	29
3.5	Summary of results of planar FSS with CR	30
3.6	Comparison between indoor tag landmarks of this work and [11]	32
4.1	Design parameters for the two cross-dipole spherical FSSs	40
4.2	Summary of results of spherical FSSs	46